



Published in final edited form as:

Cell Rep. 2020 June 02; 31(9): 107701. doi:10.1016/j.celrep.2020.107701.

Epigenetic Reprogramming of Cancer-Associated Fibroblasts Deregulates Glucose Metabolism and Facilitates Progression of Breast Cancer

Lisa M. Becker^{1,12}, Joyce T. O'Connell^{2,12}, Annie P. Vo^{2,12}, Margo P. Cain¹, Desiree Tampe³, Lauren Bizarro^{1,2}, Hikaru Sugimoto^{1,2}, Anna K. McGow⁴, John M. Asara^{5,6}, Sara Lovisa¹, Kathleen M. McAndrews¹, Rafal Zielinski⁷, Philip L. Lorenzi⁸, Michael Zeisberg³, Sughra Raza⁴, Valerie S. LeBleu^{1,2,9,13,*}, Raghu Kalluri^{1,2,10,11,*}

¹Department of Cancer Biology, Metastasis Research Center, University of Texas MD Anderson Cancer Center, Houston, TX 77054, USA

²Division of Matrix Biology, Department of Medicine, Beth Israel Deaconess Medical Center and Harvard Medical School, Boston, MA 02215, USA

³Department of Nephrology and Rheumatology, Göttingen University Medical Center, Georg August University, Göttingen 37075, Germany

⁴Department of Radiology, Brigham and Women's Hospital, Boston, MA 02215, USA

⁵Division of Signal Transduction, Beth Israel Deaconess Medical Center, Boston, MA 02215, USA

⁶Department of Medicine, Harvard Medical School, Boston, MA 02215, USA

⁷Department of Experimental Therapeutics, University of Texas MD Anderson Cancer Center, Houston, TX 77054, USA

⁸Metabolomics Core Facility, Department of Bioinformatics & Computational Biology, University of Texas MD Anderson Cancer Center, Houston, TX 77030, USA

⁹Feinberg School of Medicine, Northwestern University, Chicago, IL 60611, USA

¹⁰Department of Bioengineering, Rice University, Houston, TX 77030, USA

¹¹Department of Molecular and Cellular Biology, Baylor College of Medicine, Houston, TX 77030, USA

¹²These authors contributed equally

¹³Lead Contact

*Correspondence: valerie.lebleu@northwestern.edu (V.S.L.), rkalluri@mdanderson.org (R.K.).

AUTHOR CONTRIBUTIONS

Conceptualization, L.M.B., J.T.O., A.P.V., K.M.M., V.S.L., and R.K.; Methodology, L.M.B., J.T.O., A.P.V., and V.S.L.; Investigation, L.M.B., J.T.O., A.P.V., M.P.C., D.T., L.B., H.S., S.L., and V.S.L.; Writing – Original Draft, L.M.B., J.T.O., A.P.V., V.S.L., and R.K.; Writing – Review & Editing, L.M.B., V.S.L., and R.K.; Funding Acquisition, R.K.; Resources, A.K.M., S.R., R.Z., P.L.L., and J.M.A.; Supervision, M.Z., S.R., J.M.A., V.S.L., and R.K.

SUPPLEMENTAL INFORMATION

Supplemental Information can be found online at <https://doi.org/10.1016/j.celrep.2020.107701>.

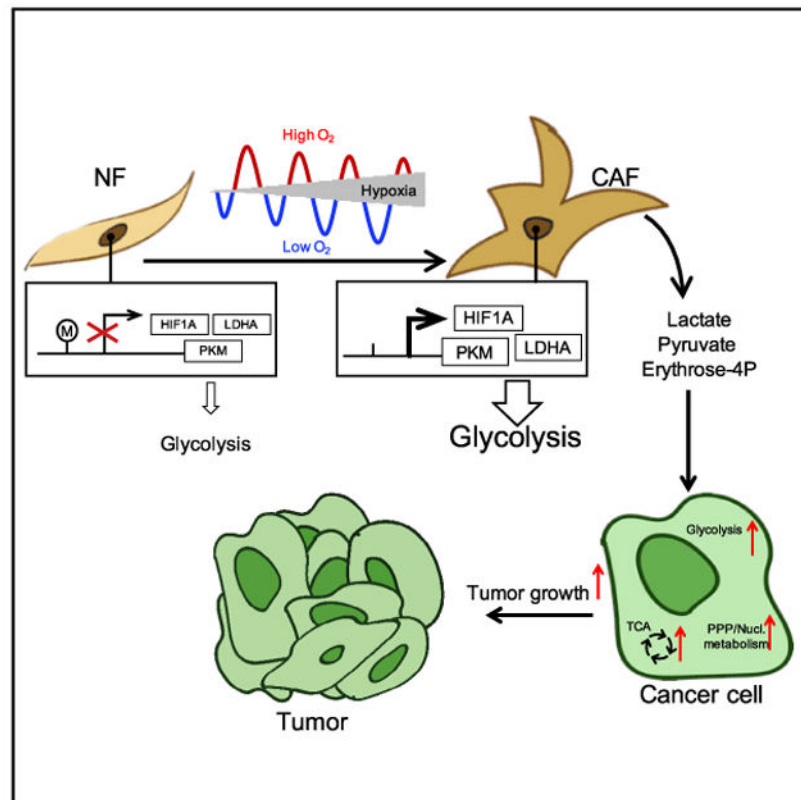
DECLARATION OF INTERESTS

The authors declare no competing interests.

SUMMARY

The mechanistic contributions of cancer-associated fibroblasts (CAFs) in breast cancer progression remain to be fully understood. While altered glucose metabolism in CAFs could fuel cancer cells, how such metabolic reprogramming emerges and is sustained needs further investigation. Studying fibroblasts isolated from patients with benign breast tissues and breast cancer, in conjunction with multiple animal models, we demonstrate that CAFs exhibit a metabolic shift toward lactate and pyruvate production and fuel biosynthetic pathways of cancer cells. The depletion or suppression of the lactate production of CAFs alter the tumor metabolic profile and impede tumor growth. The glycolytic phenotype of the CAFs is in part sustained through epigenetic reprogramming of HIF-1 α and glycolytic enzymes. Hypoxia induces epigenetic reprogramming of normal fibroblasts, resulting in a pro-glycolytic, CAF-like transcriptome. Our findings suggest that the glucose metabolism of CAFs evolves during tumor progression, and their breast cancer-promoting phenotype is partly mediated by oxygen-dependent epigenetic modifications.

GRAPHICAL ABSTRACT



In Brief

Becker et al. demonstrate that CAFs present with a pro-glycolytic phenotype, which helps to fuel the metabolism of breast cancer cells and promotes tumor growth. Chronic hypoxia induces the metabolic rewiring of normal fibroblasts toward a CAF-like, pro-glycolytic phenotype. These

microenvironmental changes enabled the epigenetic alterations and expression of key glycolytic enzymes in CAFs.

INTRODUCTION

Fibroblasts are mesoderm-derived cells readily adaptable to tissue culture expansion *ex vivo* (Alkasalias et al., 2018; Kalluri, 2016b; LeBleu and Kalluri, 2018; LeBleu and Neilson, 2020). Fibroblasts contribute to connective tissue physiology, yet their complex and dynamic roles in the pathological response associated with tissue injury repair are not fully understood (Kalluri, 2016b; LeBleu and Neilson, 2020; Micallef et al., 2012). This is of particular interest in carcinomas, wherein the accumulation of cancer-associated fibroblasts (CAFs) in tumors suggests a functional contribution of CAFs to tumor development (de Kruijf et al., 2011; Dennison et al., 2016; LeBleu and Kalluri, 2018; Moorman et al., 2012; Trimboli et al., 2009), possibly offering alternative targets for the control of cancers, including breast cancer (Hu and Polyak, 2008). Breast CAFs are a diverse population of mesenchymal cells identified by various protein markers (Costa et al., 2018; Kalluri, 2016b; Sugimoto et al., 2006; Tchou et al., 2012). The precise functional contribution of CAFs in cancer initiation and progression is under investigation, and reports support both pro- and anti-tumor properties, underscoring their complex biology in cancer (Kalluri, 2016a; Monteran and Erez, 2019). The *in vitro* expansion of CAFs enriches for cancer-promoting CAFs, evidenced by admixing experiments involving cancer cells and cultured CAFs that invariably give rise to faster growing tumors when compared to cancer cells injected by themselves or together with normal fibroblasts (NFs) (Orimo et al., 2005; Tyan et al., 2011). *In vitro* CAFs present with phenotypic features that are maintained despite long-term culture, possibly because of epigenetic reprogramming (Du and Che, 2017). Recent evidence points to an epigenetic switch involving differential DNA methylation in CAFs that may promote their pro-invasive phenotype (Albregues et al., 2015; Zhang et al., 2015).

One example of a tumor-promoting program of CAFs is their function as metabolic support cells for proliferating cancer cells (Chaudhri et al., 2013; Fiaschi et al., 2012; Guido et al., 2012; Lisanti et al., 2013; Liu et al., 2015; Martinez-Outschoorn et al., 2014; Mitchell and Engelbrecht, 2017; Romero et al., 2015; Sanford-Crane et al., 2019; Zhang et al., 2015). Highly proliferative cells (cancer cells) present with enhanced glycolytic rates, metabolizing glucose to lactate, regardless of oxygen availability (Warburg effect). Enhanced glycolysis supports the increased demand for biosynthetic products necessary for cancer cell growth and multiplication (Pavlova and Thompson, 2016; Vander Heiden and DeBerardinis, 2017). Similarly, CAFs have been proposed to undergo metabolic reprogramming toward aerobic glycolysis and participate in a tumor-promoting lactate shuttle with cancer cells (reverse Warburg effect) (Fiaschi et al., 2012; Guido et al., 2012; Pavlides et al., 2009; Roy and Bera, 2016).

A key feature of metabolic reprogramming in tumors is the glycolytic reprogramming by hypoxia and hypoxia-inducible factor 1 alpha (HIF-1 α) (Fiaschi et al., 2012; Zhang et al., 2015), which directly induces the transcription of glycolytic enzymes (Semenza, 2010). Furthermore, demethylation of the hypoxia response element in the *HIF1A* promoter region

can result in its auto-transactivation (Koslowski et al., 2011). A growing hypoxic tumor is associated with elevated HIF-1 α that may influence the secretome (Ammirante et al., 2014) and glucose metabolism of CAFs (Madsen et al., 2015; Zhang et al., 2015); however, the mechanistic underpinning of sustained metabolic reprogramming of CAFs remains unknown. Our study of human and mouse CAFs and NFs uncovered that dynamic changes in oxygen levels likely induce epigenetic changes (*HIF1A* promoter hypomethylation, among others) that control metabolic reprogramming in CAFs toward increased glycolysis.

RESULTS

α SMA⁺ CAFs Promote Mammary Tumor Growth and Display Enhanced Glycolysis

We evaluated the functions of a dominant CAF population in mammary carcinoma. α -Smooth muscle actin (α SMA)-expressing mesenchymal cells accumulate in human breast cancer tissues and animal models of mammary carcinoma (Sugimoto et al., 2006; Tchou et al., 2013). In the metastatic 4T1 murine mammary tumor model, CAFs in primary tumors express various markers, predominantly α SMA, as well as fibroblast specific protein-1 (FSP1, S100A4) in a distinct CAF subset (Sugimoto et al., 2006). We previously reported on the role of FSP1⁺ CAFs in promoting the metastatic outgrowth of breast cancer cells, involving vascular endothelial growth factor-A (VEGF-A)-dependent angiogenic remodeling of the metastatic niche (O'Connell et al., 2011). Using transgenic mice that enable the capture of FSP1⁺ and α SMA⁺ CAFs and stromal cells in breast tumors and healthy mammary fat pads, we observed distinct, minimally overlapping FSP1⁺ and α SMA⁺ stromal cells and CAFs. Specifically, 4T1 orthotopic tumor-bearing and healthy *S100A4-GFP* and *α SMA-RFP* mice were evaluated for GFP and red fluorescent protein (RFP) expression, measuring *S100A4* (FSP1) and α SMA (*Acta2*) promoter activity, respectively. Stromal cells were defined as live cells positive for at least one of the two fluorescent proteins (Figure S1A). α SMA⁺ stromal cells, relative to FSP1⁺ stromal cells, were more abundant in the mammary fat pads (MFPs; ~62% α SMA⁺) and lungs (~80% α SMA⁺) of healthy mice, as well as in tumors (~94% α SMA⁺) and metastatic lungs (~66% α SMA⁺) of 4T1 tumor-bearing mice. FSP1⁺ cells were also noted in these tissues, albeit at relatively lower frequencies (~22% in MFPs, ~17% in lungs, ~2% in 4T1 tumors, and ~28% in metastatic lungs) (Figure S1B). Stromal cells or CAFs (in the case of tumors and metastatic lungs) double positive for α SMA and FSP1 were infrequent, in agreement with our previous findings (Sugimoto et al., 2006) and direct visualization of GFP (FSP1) and RFP (α SMA) in tissue sections (Figure S1C).

To measure the rate-limiting role of α SMA⁺ CAFs in breast cancer progression, the growth kinetics and metastatic potential of orthotopically implanted 4T1 cells were evaluated in α SMA-viral thymidine kinase (vTK) transgenic mice. In these mice, the continuous administration of ganciclovir (GCV) enables the specific depletion of proliferating α SMA⁺ CAFs, on the basis of *Acta2* gene promoter-driven expression of the vTK transgene (LeBleu et al., 2013a; Özdemir et al., 2014). The depletion of α SMA⁺ CAFs was initiated when tumors were firmly established (~500 mm³), and the pressure to limit CAF accumulation via GCV administration was continued until the experimental endpoint (Figure 1A). α SMA⁺ CAF depletion resulted in a significant reduction in primary tumor growth (Figures 1A-1C,

S2A, and S2B), albeit the metastatic burden was unchanged or enhanced (Figures 1D-1F and S2B). This approach does not directly affect cancer cells, which are deprived from expressing the transgene. Body weight was not affected by α SMA⁺ CAF depletion (Figure S2B). α SMA⁺ CAF depletion exacerbated primary tumor hypoxia (carbonic anhydrase 9 [CAIX]; Figure S3A) and diminished blood (CD31) and lymphatic angiogenesis (Lyve1; Figures S3B and S3C). Pericyte coverage of the blood vessels remained unchanged (CD31 associated with platelet-derived growth factor receptor β [PDGFR β]; Figure S3B). However, perivascular α SMA expression increased (Figure S3B), supporting that the depletion strategy primarily affects proliferating CAFs rather than possibly more quiescent perivascular cells. These findings also imply that reduced tumor angiogenesis is an indirect consequence of α SMA⁺ CAFs depletion. The results were recapitulated in the MMTV-PyMT (PyMT) mammary carcinoma animal model (Fantozzi and Christofori, 2006; Lin et al., 2003). In PyMT mice bred with α SMA-vTK mice (generating PyMT; α SMA-vTK mice), α SMA⁺ CAF depletion via GCV administration led to significantly reduced tumor growth (Figure S4A). PyMT tumors orthotopically transplanted onto the α SMA-vTK background also displayed significant tumor growth reduction when subjected to the depletion of α SMA⁺ CAFs (Figure 1G), supporting that the genetic strategy primarily affected α SMA⁺ CAFs in the host response rather than cancer cells. In PyMT models, the depletion of α SMA⁺ CAFs resulted in a significant primary tumor growth reduction (Figures 1G, S4A, S4D, and S4F) similar to that of 4T1 orthotopic tumors (Figures 1A-1C, S2A, and S2B), and the metastatic burden was unchanged, despite smaller primary tumors (Figures S4B and S4C). Despite smaller tumor volumes, α SMA⁺ CAF-depleted PyMT tumors displayed similar hypoxia levels than larger control tumors (Figure S4E), and angiogenesis was reduced with the depletion of α SMA⁺ CAFs, without affecting perivascular coverage (Figure S4F). These results point to a primary tumor growth-promoting role for α SMA⁺ CAFs in mammary carcinomas. Despite the significant decrease in primary tumor growth upon the depletion of α SMA⁺ CAFs, lung metastases in the invasive breast cancer models studied were similar or enhanced (*vide supra*). Metastatic disease was rarely seen at the time of GCV initiation in the 4T1 orthotopic model (Figures 1E-F), and the depletion of α SMA⁺ CAFs in a 4T1 lung colonization experiment (intravenously injected 4T1 cells) did not affect lung tumor growth (Figure 1H). These results support the idea that the function of α SMA⁺ CAFs in breast cancer progression was primarily realized by promoting primary tumor growth.

Recent studies suggest an altered metabolism of CAFs (Chaudhri et al., 2013; Fiaschi et al., 2012; Guido et al., 2012; Migneco et al., 2010; Mitchell and Engelbrecht, 2017; Pavlides et al., 2009; Roy and Bera, 2016). We measured metabolite accumulation in control and α SMA⁺ CAF-depleted 4T1 tumors. α SMA⁺ CAFs depletion was associated with decreased metabolite accumulation (Figure 1I), including suppressed glycolysis and nucleic acid metabolism, with a decrease in the metabolites associated with glycolysis, tricarboxylic acid (TCA) cycle, pentose phosphate pathway (PPP), and nucleotide metabolism. To test whether the depletion of α SMA⁺ CAFs affected glycolysis in cancer cells, wild-type (WT) and α SMA-vTK 4T1 tumor tissues were immunolabeled for CK8 (to label cancer cells) and pyruvate kinase M2 (PKM2), hexokinase 2 (HK2), and glucose transporter 1 (GLUT1). While PKM2 expression in cancer cells was decreased, CK8-specific GLUT1 and HK2 expression remained unchanged (Figures S3D-S3F). To determine metabolic shifts in CAFs,

we purified and cultured 4T1-tumor derived CAFs (murine CAFs [mCAF_s]) and fibroblasts derived from healthy murine mammary tissue (murine NFs [mNF_s]). We observed elevated transcript levels for metabolic enzymes in mCAF_s compared to mNF_s, including Glut1 (*Slc2a1*), *Hk2*, *Pkm1/2* (*Pkm*), phosphofructokinase L (*Pfkf*), lactate dehydrogenase a (*Ldha*), and monocarboxylate transporter-4 (MCT4, *Slc16a3*) (Figure 1J). Metabolomic profiling of mCAF_s and mNF_s showed increased metabolite accumulation in mCAF_s (Figure 1K). Key metabolites associated with glycolysis and the TCA cycle were found to be relatively increased in mCAF_s (Figure 1L), supporting the notion that mCAF_s present with enhanced glycolytic activity when compared to mNF_s. Pymt tumor-derived mCAF_s showed enhanced glycolysis compared to mNF_s, with an increase in the gene expression of metabolic enzymes (Figure S4G) and a moderate increase in the extracellular acidification rate (ECAR) upon the addition of glucose and oligomycin, the latter maximizing glycolysis by inhibiting mitochondrial respiration (Figure S4H).

Lactate Shuttle between CAFs and Cancer Cells Promotes Tumor Growth

Studies suggest a lactate shuttle between CAFs and cancer cells in the tumor microenvironment (TME) (Fiaschi et al., 2012; Lisanti et al., 2013; Martinez-Outschoorn et al., 2014). To measure the impact of a lactate shuttle between CAFs and cancer cells, we engineered 4T1 cancer cells with reduced MCT1 expression (Figures 2A and 2B). Reduced *Slc16a1* (MCT1) expression in 4T1 cells impaired orthotopic tumor growth (Figures 2B-2D), but metastasis was unchanged (Figure 2E). The loss of *Slc16a1* in 4T1 cells (Figures 2B-2D) did not affect the recruitment of α SMA⁺ CAFs into the tumors or tumor vasculature (Figures 2F, S5A, and S5B). These results support the idea that limiting lactate uptake in cancer cells inhibits tumor growth without limiting CAF accumulation.

To identify the specific functional role of CAF-derived lactate as fuel for cancer cells, we evaluated the growth of 4T1 orthotopic tumors co-implanted with fibroblasts with suppressed lactate production. The suppression of pyruvate dehydrogenase kinase 4 (*Pdk4*) in α SMA⁺ fibroblasts (mouse embryonic fibroblasts [MEF_s]) resulted in the combined downregulation of multiple PDK isoforms compared to control scrambled small hairpin RNA (shRNA; shScrbl) (Figure 2G), and shPdk4-MEF showed reduced lactate production compared to controls (Figure 2H). Co-injection of 4T1 cancer cells with shPdk4-MEF blunted tumor growth compared to controls (4T1 cells injected with shScrbl-MEF; Figures 2I and 2J). Metabolomic analyses of tumors and cancer cells fluorescence-activated cell sorting (FACS) purified from tumors revealed a decrease in metabolite accumulation in shPdk4-MEF tumors and cancer cells when compared to controls (Figures 2K and 2L). α SMA⁺ CAF numbers and proliferation, hypoxia, angiogenesis, and pericyte coverage remained unchanged in 4T1 + shPdk4-MEF tumors compared to control tumors (Figures S5C-S5E), supporting the notion that the enhanced glycolytic activity of CAFs promotes tumor growth via lactate transfer to cancer cells.

Breast Cancer-Derived Human CAFs Display Enhanced Glycolytic Activity

We evaluated the metabolic rewiring of human breast CAFs and established a catalog of fibroblasts cultured from image-guided biopsies of breast tissue from women undergoing imaging evaluation of clinical and/or screen-detected breast abnormalities (Figure 3A; Table

S1). Tissues were clinically evaluated for pathological diagnosis and collected for further analyses. Based on histopathological criteria, the samples were stratified into cancer and non-cancer groups. The study comprised predominantly white (78.4%) adult women with a median age of 51 years (Table S1). The clinical pathology diagnosis revealed that 34% (n = 172) presented with cancer and 66% (n = 327) had normal breast tissue or non-neoplastic lesions (Figure 3A; Table S1). Non-cancer (benign) cases included fibroadenomas and benign cysts and/or calcification, whereas cancer cases were predominantly invasive carcinomas, notably invasive ductal (IDC) and invasive carcinoma with ductal and lobular features (IDLC) (Figure 3A; Table S1). Both benign and cancer cases presented with a similar relative proportion of mammographic tissue density (Figure 3A). Immunolabeling showed distinct stromal composition between cancer and benign breast tissue, with enhanced collagen I, collagen III, tenascin C (TNC), α SMA, and FSP1, and decreased laminin 1 expression in IDCs and IDLCs compared to benign lesions (Figure 3B; Data S1). Although microvascular density was enhanced in IDC and IDLC cases compared to benign lesions, NG2⁺ pericyte coverage of these vessels was reduced (Figure 3B; Data S1), in agreement with our previous findings (Cooke et al., 2012; Kim et al., 2016).

Fibroblasts from ~39% of all of the samples were successfully expanded in culture, and the ease in the propagation of fibroblasts *in vitro* did not indicate any bias with respect to pathology or mammographic density parameters (Figure 3C; Table S1). All of the subsequent analyses were performed on low passage fibroblast cultures (<20 passages), and a selected number of lines were used for in-depth analyses (Table S2). The biopsy-derived fibroblasts were thereafter referred to as CAFs if derived from breast neoplasms (human CAFs [hCAFs]), or benign fibroblasts if derived from benign breast tissue (human benign fibroblasts [hBFs]) (Figures 3A-3C). Transcript levels for *PFKL*, *PKM*, *HK2*, *SLC2A1* (encoding GLUT1), *phosphofructokinase M (PFKM)*, and *SLC16A4* (encoding MCT4), were elevated in hCAFs compared to hBFs and reduced for fructose-1,6-bi-sphosphatase (*FBP1*) (Figure 4A). Lactate production was increased in hCAF conditioned medium (CM) compared to hBF CM (Figure 4B). ECAR was significantly increased in hCAFs compared to hBFs (Figure 4C). hCAFs also exhibited increased glycolysis, glycolytic capacity, and glycolytic reserve when compared to hBFs (Figure 4D), supporting a pronounced pro-glycolytic phenotype of hCAFs. Targeted mass spectrometry analyses revealed metabolite enrichment indicative of increased glycolysis, aminosugar metabolism, TCA cycle, PPP, nucleotide metabolism, amino acid (aa) metabolism, and urea cycle in hCAFs compared to hBFs (Figures 4E and 4F). The results support that cultured hCAFs and mCAFs demonstrate a pro-glycolytic transcriptome and metabolome compared to BF, and such acquired features are maintained even after passaging the cells, suggesting that the observed metabolomic changes may be imprinted in the CAF genome.

Cancer Cells Uptake and Use CAF-Secreted Metabolites to Fuel Their Metabolism

To define the metabolic exchange between CAFs and cancer cells, we evaluated the fate of labeled metabolites in cancer cells fed with the metabolic products of CAFs. Uniformly labeled ¹³C glucose ([U-¹³C] glucose) was fed to hCAFs (48 h), and utilization of glucose by hCAFs was evidenced by labeled metabolites implicated in glycolysis, the TCA cycle, PPP, nucleotide metabolism, aa metabolism, and urea cycle (Figure 5A). Next, hCAFs were

fed [$U\text{-}^{13}\text{C}$] glucose for 48 h before cells were washed and cultured for 48 h in unlabeled glucose media (Figure 5B). The hCAF-secreted labeled metabolome (conditioned media [CM]) revealed metabolites involved in PPP, the TCA cycle, and nucleotide metabolism (Figure 5C). The CM containing hCAF-labeled metabolites was also used to feed human breast cancer MDA-MB-231 cells for 24 h (Figure 5B). MDA-MB-231 cells were harvested, and the ^{13}C labeled metabolites derived from these cells were measured (Figure 5D). The analysis indicated that hCAF-derived metabolites were used by cancer cells to fuel PPP and nucleotide metabolism (Figure 5D). These experiments indicate that human cancer cells use hCAF-derived metabolites to fuel their metabolic activity, specifically nucleic acid metabolism.

Rate-Limiting Enzymes of Glycolysis Are Epigenetically Modified in Breast CAFs

The pro-glycolytic metabolism of hCAFs was maintained despite repeated *in vitro* passages in atmospheric oxygen (21% O_2). Transcriptomic and metabolomic analyses and elevated ECAR in hCAFs (compared to hBFs) support the pro-glycolytic phenotype of hCAFs in identical culture conditions of hBFs (Figures 4 and 5A). We explored whether epigenetic modification could explain the maintained metabolomic changes in cultured hCAFs. We noted that the promoters of rate-limiting glycolytic genes *FBP1*, *PKM*, and *LDHA* (Doherty and Cleveland, 2013; Liu and Vander Heiden, 2015) were differentially methylated in hCAFs (Figure 6A). *FBP1* opposes glycolysis by catalyzing the hydrolysis of fructose-1,6-bi-sphosphate to fructose-6-phosphate, whereas *PKM* promotes glycolysis by catalyzing the conversion of phosphoenolpyruvate to pyruvate, and *LDHA* catalyzes the conversion of pyruvate to lactate. Methylated DNA immunoprecipitation (MeDIP) and bisulfite conversion assays showed hypermethylation of the *FBP1* gene promoter in hCAFs compared to hBFs (Figures 6A and S6A). In contrast, *PKM* and *LDHA* gene promoters were hypomethylated in hCAFs compared to hBFs, as determined by MeDIP (Figure 6A).

HIF-1 α directly regulates the transcription of *PKM* and *LDHA*, and *FBP1* exerts repressing functions on HIF-1 α activity (Li et al., 2014). Despite identical culture conditions, both HIF-1 α transcript and protein levels were elevated in hCAFs compared to hBFs (Figures 6B and 6C; Data S2). MeDIP revealed *HIF1A* promoter hypomethylation in hCAFs compared to hBFs (Figure 6D). When exposed to the demethylating agent 5-azacytidine (5-Aza), hBFs showed increased *LDHA*, *HIF1A*, and *PKM* transcript levels, suggesting the epigenetic regulation of pro-glycolytic genes in fibroblasts (Figure 6E). These results support the idea that the hypomethylation of *HIF1A*, *PKM* and *LDHA* and the hypermethylation of *FBP1* could contribute to sustaining the pro-glycolytic program of CAFs.

Oscillating Oxygen Tension Results in Epigenetic Reprogramming of hBFs to Attain CAF-like Metabolic Profiles

Chronic hypoxia is a feature of growing tumors, leading to the stabilization of HIF-1 α . We hypothesized that chronic hypoxia may initiate HIF-1 α -mediated metabolic reprogramming of CAFs due to promoter hypomethylation, resulting in sustained elevation of HIF-1 α levels in hCAFs compared to hBFs (Figures 6B and 6C). To test this hypothesis, hBFs from 3 distinct patients were subjected to increasing intervals of hypoxia (1% O_2) for 1,3,5, and 7 days, followed by 48 h of reoxygenation (21% O_2) for each time point. In prolonged

hypoxia (5 and 7 days), HIF-1 α protein expression in hBFs was elevated despite re-oxygenation (Figures 7A and S7A; Data S2). *HIF1A* transcripts were elevated in 2 of the 3 hBF lines upon hypoxia exposure and remained increased upon re-oxygenation (Figures 7B and S7B). *HIF1A* promoter hypomethylation was observed in hBFs subjected to prolonged hypoxia (120 h), and it remained hypomethylated upon re-oxygenation (120 h hypoxia followed by 24 h of re-oxygenation) (Figures 7C and S6B). These findings agree with the elevated HIF-1 α transcript and protein levels noted in hBFs subjected to hypoxia/re-oxygenation experiments (Figures 7A, 7B, S7A, and S7B). Furthermore, increased exposures of hBFs to hypoxia followed by re-oxygenation elevated the normoxic baseline transcript levels of *HIF1A*, *SLC2A1*, *HK2*, *PFKL*, *PKM*, and *LDHA* (Figures 7D, 7E, and S7C). To determine whether increasing intratumoral hypoxia in growing tumors contributes to the accumulation of glycolytic CAFs *in vivo*, we evaluated the glycolytic profiles of CAFs in hypoxic and normoxic tumor regions. Glycolytic CAFs, defined by the co-expression of α SMA and PKM2 or HK2, were more abundant in hypoxic (CAIX high) rather than normoxic (CAIX low) areas of Pymt tumors (Figure 7F). α SMA⁺ CAFs expressing FBP1 were found in both normoxic and hypoxic tumor areas (Figure 7F). In both Pymt and 4T1 tumors, larger tumor volumes were partly associated with increased hypoxia and significant accumulation of glycolytic CAFs (α SMA/PKM2) (Figures S7D and S7E). In 4T1 tumors, α SMA/HK2 CAFs also significantly expanded with tumor growth. While less glycolytic CAFs (α SMA/FBP1) remained unchanged in 4T1 tumors, in Pymt tumors, this population significantly decreased as tumor volumes increased (Figures S7D and S7E). Lastly, patient tissues revealed a significant increase in hypoxia-associated fibroblasts (α SMA⁺CAIX⁺) in tumor samples (IDC) compared to benign tissues (Figure 7G). These results inform us about the role of chronic hypoxia in inducing persistent epigenetic changes that promote a pro-glycolytic program in CAFs.

DISCUSSION

Using transgenic mice and multiple, complementary mouse models of breast cancer with altered CAFs content and CAFs or cancer cell metabolism, we identified the role of α SMA⁺ CAFs in promoting mammary tumor growth by fueling cancer cell metabolism. Tumor growth was reduced when α SMA⁺ CAFs were genetically depleted, yet metastasis was unchanged (or enhanced). The similar metastatic burden in α SMA⁺ CAFs-depleted tumor-bearing mice compared to control mice is significant because despite ~50% primary tumor reduction, metastases could still develop unhindered, suggesting that cancer cells likely gained a pro-metastatic potential, or the remaining cancer cells were able to seed the lung at the same rate as the control tumors. Our genetic strategy to deplete α SMA⁺ CAFs did not affect metastatic outgrowth (lung colonization assay), suggesting a more dominant role for these cells in the primary tumor. This was manifested principally by increased intratumoral hypoxia and suppressed angiogenesis upon α SMA⁺ CAFs depletion.

Profiling of murine and human CAFs, compared to their normal counterparts, revealed a pro-glycolytic phenotype of CAFs, as previously suggested (Koukourakis et al., 2006; Pavlides et al., 2009; Migneco et al., 2010). Pymt-derived mCAFs show a less pronounced glycolytic phenotype than 4T1-derived mCAFs, demonstrating heterogeneity between different animal models. The differences are likely due to higher hypoxia levels in 4T1

tumors compared to Pymt tumors of similar volume, which is in line with our observations of hypoxia-induced metabolic reprogramming of CAFs. Depleting α SMA⁺ CAFs in tumors mimicked growth kinetic phenotypes observed when pro-glycolytic metabolism of CAFs was impaired or when lactate uptake by cancer cells was suppressed. Although we noted several metabolic pathways upregulated in CAFs, we focused on glycolysis, as the CAF glycolytic phenotype had been proposed by multiple, mainly *in vitro* studies (Fiaschi et al., 2012; Rattigan et al., 2012; Sanford-Crane et al., 2019; Whitaker-Menezes et al., 2011). PDKs are involved in both metabolic reprogramming of cells (suppressing oxidative phosphorylation) and upregulation of HIF-1 α ; therefore, they participate in a feedforward loop to induce the Warburg phenotype in cancer cells (Liu et al., 2014; McFate et al., 2008). In CAFs and cancer cells, PDKs promote lactate production (Liu et al., 2014). Knockdown of *Slc16a1* (MCT1) was shown to inhibit prostate cancer growth *in vivo* (Fiaschi et al., 2012). Our findings agree with these studies and support a lactate shuttle between CAFs and cancer cells in mammary tumors, with an impact on tumor progression. In our experiments, shPDK4 MEFs were unlabeled, which did not allow us to study the fate of these engineered fibroblasts *in vivo*. Nonetheless, *in vivo* admixture experiments involving fibroblasts and cancer cells are commonly used to study fibroblast function in tumor progression and suggest the sufficient survival of implanted fibroblasts (Borriello et al., 2017; Orimo et al., 2005). Our metabolomic analyses of tumors with glycolysis-impaired CAFs informed us that the pro-glycolytic phenotype of CAFs supports cancer cells and tumor growth *in vivo*. The tumor-promoting role of α SMA⁺ CAFs in mammary carcinoma is also associated with TME remodeling, with CAF depletion impeding tumor angiogenesis and enhancing intratumoral hypoxia.

In addition to a CAFs-cancer cell lactate shuttle, our metabolite transfer experiment indicates that CAF-secreted metabolites fuel the biosynthetic processes of cancer cells, specifically PPP and nucleotide metabolism. While it remains unknown whether the uptake of CAF-derived metabolites by cancer cells could be influenced when nutrients are scarce, our experiments describe the basal metabolic relationship between CAFs and cancer cells and show the uptake of CAFs-derived metabolites by cancer cells, which was principally noted in biosynthetic pathways. For instance, erythrose-4-phosphate was found in the CAF secretome, which can be taken up by cancer cells and fuel PPP by conversion into sedoheptulose-7-phosphate and phosphoribosyl pyrophosphate (PRPP) (Stincone et al., 2015), and both of these metabolites were found labeled in cancer cells fed with ¹³C-labeled CAF CM. Therefore, cancer cells likely present with scavenging properties that enable the efficient uptake of metabolites secreted by other cells, including CAFs, thus effectively hijacking metabolites in the TME to support their growth and survival (Mitchell and Engelbrecht, 2017). Finally, CAF-depleted tumors show reduction in metabolites participating in PPP and nucleotide metabolism, adding support for the role of CAFs in fueling the PPP and nucleotide metabolism of cancer cells. The expression of glycolytic enzymes by cancer cells upon the depletion of CAFs was moderately decreased. High intratumoral hypoxia in CAF-depleted tumors likely elevates cancer cell glycolysis, thereby possibly masking greater effects of CAF depletion on the metabolism of cancer cells (Fiaschi et al., 2012; Semenza, 2010; Zhang et al., 2015).

In our metabolomic studies, lactate was not among the top CAF-secreted metabolites. Although lactate was noted in the CAF secretome, a high false-positive detection rate of labeled lactate in the control unlabeled CAFs (>5%) rendered its detection inconclusive as a CAF-secreted metabolite. Increased lactate secretion was, however, confirmed with other assays, including the glycolysis stress test. In the metabolite transfer experiment, pyruvate was the second-most abundant CAFs-secreted metabolite. Previous studies suggest growth stimulatory effects of pyruvate on cancer cells by fueling their mitochondrial respiration (Diers et al., 2012). Gui et al. (2016) showed that pyruvate taken up by cancer cells is converted to lactate to increase the intracellular NAD⁺ level, which is lowered by metformin treatment, thereby rendering cancer cells resistant to metformin. Since lactate as well as pyruvate can be transferred via MCT1, these reports also agree with our findings using cancer cells with *Slc16a1* (MCT1) knockdown, and both a lactate and pyruvate shuttle between CAFs and cancer cells may fuel cancer cell metabolism. Knockdown of PDK4 was shown to decrease HIF1- α and PKM2 expression in cancer cells, and the overexpression of PDK4 in fibroblasts was accompanied by an increase in HIF1- α and PKM2 (Liu et al., 2014). This suggests that pyruvate production may also be impaired in fibroblasts with PDK4 knockdown in our experiments. Whether pyruvate is secreted through MCT4 or whether CAFs upregulate additional monocarboxylate transporters for pyruvate secretion remains to be investigated.

We identified the hypoxia-induced epigenetic rewiring of fibroblasts that promotes a pro-glycolytic phenotype and results in the sustained elevation of *HIF1A*, *PKM*, and *LDHA* and the suppression of *FBP1* gene expression. This seems to be facilitated by changes in the DNA methylation status of specific metabolic gene promoters. Despite *LDHA* promoter hypomethylation, gene expression was not significantly increased in hCAF. This may be due to patient heterogeneity, and an increased n number may be needed to achieve statistical significance in gene expression. We uncovered that chronic hypoxia results in *HIF1A* hypomethylation in fibroblasts. Fibroblasts and cancer cells in growing tumors are exposed to chronic hypoxia, creating an opportunity for metabolic coupling, coordinated by epigenetic events that favor the accumulation of pro-glycolytic CAFs with pro-tumorigenic properties. The accumulation of pro-glycolytic CAFs in regions of increased intratumoral hypoxia supports this notion. Hypoxia has been shown to reduce the levels of the methyl donor S-adenosylmethionine (Liu et al., 2011). HIF-1 α directly regulates the transcription of *PKM* and *LDHA*, and the hypomethylation of *PKM* is particularly intriguing. PKM2 can bind and transactivate HIF-1 α in the nucleus, where it is recruited along with HIF-1 α and JMJD5 to the *LDHA* and *PKM2* loci to induce metabolic transcriptional reprogramming (Luo et al., 2011; Wang et al., 2014). Furthermore, the non-catalytic domain of FBP1 can exert repressing functions on HIF-1 α activity (Li et al., 2014). Our data support these results and further highlight a potent circuitry in metabolic rewiring of cells that implicate *HIF1A*, *PKM1/2*, *LDHA*, and *FBP1*. It is also noted that FBP1 and PKM1/2 present with non-canonical functions (Huangyang and Simon, 2018), which may also play a role in fibroblast reprogramming in tumors.

Although not studied here, it is possible that the increased hypoxia in α SMA⁺ CAF-depleted tumors influenced cancer cell dissemination by affecting their metabolism (Rankin and Giaccia, 2016). In contrast to the increased intratumoral hypoxia upon the depletion of

CAFs, the increase in intratumoral hypoxia in growing tumors, imposed by inadequate angiogenesis, promotes the emergence of epigenetically modified, pro-glycolytic CAFs that may, at least in part, fuel cancer cell biosynthetic needs. Here, we show that chronic exposure to hypoxia of hBFs was sufficient to induce a transcriptome characteristic of CAFs (pro-glycolytic) despite re-oxygenation, suggesting hyperresponsiveness to hypoxia. The catalytic domain of Tet hydroxylases is dependent on the TCA cycle intermediate α -ketogluta-rate (Branco et al., 2011). Our study supports a connection between oxygen tension and DNA methylation, possibly linking changes in TCA cycle intermediates, one-carbon metabolism, and the activity of enzymes regulating DNA methylation. It remains unknown whether specific directives enable a DNA methylation pattern that supports a pro-glycolytic phenotype of CAFs or whether CAFs with newly acquired pro-glycolytic gene methylation patterns are selected due to microenvironmental pressure, such as oxygen availability. Although our study implicates α SMA⁺ CAFs in breast cancer as tumor promoting, we also reported on the tumor-restraining properties of α SMA⁺ CAFs in distinct solid tumors (Özdemir et al., 2014). These results underscore the functional heterogeneity of CAFs and caution against assigning CAF markers with general functions across tumor types (LeBleu and Neilson, 2020).

In summary, we identify that patient-derived breast CAFs exhibit an activated metabolism with enhanced glycolytic activity, which is stabilized by epigenetic changes in key glycolytic genes, including *HIF1A*. This feature of CAF metabolism fuels cancer cells and promotes tumor growth. Therapeutic agents targeting glycolysis undergoing clinical evaluation may also function by concomitantly affecting the metabolism of pro-tumorigenic CAFs in breast cancer.

STAR★METHODS

RESOURCE AVAILABILITY

Lead contact—Further information and requests for resources and reagents should be directed to and will be fulfilled by the Lead Contact, Valerie S. LeBleu (Valerie.lebleu@northwestern.edu).

Materials availability—This study did not generate new unique reagents.

Data and Code Availability—Source data for all figures in this paper is available [Mendeley Data: <https://doi.org/10.17632/9dgjv8bt8c.1>].

EXPERIMENTAL MODEL AND SUBJECT DETAILS

Murine cell lines—4T1 BALB/c mammary tumor epithelial cells (RRID:CVCL_0125) and BALB/c mouse embryonic fibroblasts (passage 3) were grown in Dulbecco's Modified Eagle's Medium supplemented with 10% fetal calf serum and penicillin/streptomycin (each 100U/ml). In same experiments, 4T1 were modified to express GFP and luciferase (GFP luc). 4T1 cells were validated by STR analysis and confirmed negative for mycoplasma. Mouse normal mammary fibroblasts and cancer-associated fibroblasts were grown from tissues obtained from α SMA-RFP mice (previously described in LeBleu et al., 2013a;

healthy or with orthotopic 4T1 tumors), or from MMTV-PyMT (Pymt) (Fantozzi and Christofori, 2006; Lin et al., 2003) mice. Tissues were minced into 1 mm³ pieces and digested overnight in 300U Type I collagenase per ml of RPMI-1640 media containing 20% fetal bovine serum (FBS) with 100U/ml penicillin/streptomycin and 250ng/ml amphotericin (PSA) (complete media). Fibroblasts were subsequently allowed to grow out of the tissue pieces maintained in complete media. When isolated from α SMA-RFP mice, the cultured cells underwent flow activated cell sorting (FACS) to purify α SMA-RFP⁺ fibroblast populations. Mouse embryonic fibroblasts were isolated from embryos harvested at E10-13 using the same method. All cells were cultured at 37°C, 21% O₂ and 5% CO₂ unless otherwise stated in the methods. All cells were derived from female mice (with the exception of mouse embryonic fibroblasts).

Patient-derived cell lines—Human benign mammary fibroblasts and cancer-associated fibroblasts were grown from breast biopsy tissue samples obtained as part of an institutionally approved clinical study at Boston’s Brigham and Women’s Hospital. Informed consent was obtained from all subjects. The breast biopsies were either ultrasound-guided (Ultrasound core needle biopsy = US-CNB) or stereotactically-guided (Stereo-CNB) core needle biopsies. In Stereo-CNB, the biopsy target was always microcalcifications, but the core samples provided for this study did not contain calcifications, as determined by X-ray. Tissues were grouped into ‘cancer’ and ‘benign tissue’ groups based on pathological analysis. All patients (n = 499) were female and between 18 and 88 years of age (median age of 51 years). The tissues were mounted into O.C.T mounting media and frozen for subsequent immunolabeling studies or processed for fibroblast propagation. For the latter, after an ethanol and subsequent phosphate-buffered saline (PBS) wash, 1 mm³ pieces were digested overnight in 300 U Type I collagenase per ml of RPMI-1640 media containing 20% fetal bovine serum (FBS) with 100 U/ml penicillin/streptomycin and 250 ng/ml amphotericin (PSA) (complete media). Fibroblasts were subsequently allowed to grow out of the tissue pieces and maintained in complete media. MDA-MB-231 human breast cancer cells (RRID:CVCL_0062) were grown in 10% FBS, 2 mM L-glutamine, 2.5 mM glucose in DMEM. All cells were cultured at 37°C, 21% O₂ and 5% CO₂ unless otherwise stated in method details or figure legends.

In vivo animal studies—For all animal studies female virgin mice of ~8 weeks of age and of ~20-25 body weight were used. In co-implantation experiments of MEF and 4T1 cancer cells, nu/nu mice were used; mice in all other experiments were on BALB/c background. Littermate mice were randomly assigned in experimental groups. WT control mice in experiments with α SMA-vTK mice were the littermate α SMA-vTK⁻ mice of α SMA-vTK⁺ mice. Nu/nu (RRID:IMSR_CRL:088) and BALB/c mice (RRID:IMSR_CRL:028) were purchased from Charles River. MMTV-PyMT mice were purchased from Jackson Laboratories on FVB/N background (RRID:IMSR_JAX:022974) and backcrossed to BALB/c background for > 10 generations. α SMA-vTK, as well as α SMA-RFP mice were generated in our lab and previously published (LeBleu et al., 2013a, 2013b). These mice were also backcrossed to BALB/c background. FSP-GFP mice were a generous gift of Eric Neilson. All mice were housed in the institutional facilities of UT MD Anderson Cancer Center and Harvard Medical School under regular housing conditions. All

animal studies were approved by the institutional animal care and use committees of UT MD Anderson Cancer Center and Harvard Medical School.

METHOD DETAILS

Gene expression knockdown—MEF clones showing suppression of PDK isoforms were obtained by knockdown of *Pdk4* and were generated according to the manufacturer's protocol (Addgene) and using the pLKO.1 – TRC cloning vector and the following shRNA oligos:

5' CCGGTCTACTCTATGTCAGGTTATGCTCGAGCATAACCTGACATAGAGTAGATTTT
TTG 3' (Forward) and 5' AATTCAAAAATCTA

CTCTATGTCAGGTTATGCTCGAGCATAACCTG ACATAGAGTAGA 3' (Reverse).

Target sequence was 5' TCTACTCTATGTCAGGTT ATG 3'. Control scrambled shRNA oligos were 5'

CCGGGAACACGTCAGACCAGGATCACATACTCGAGTATGTGATCCTGGTCTG
ACGTGTTCTTTTTG 3' (Forward) and 5' AATTCAA

AAGAACACGTCAGACCAGGATCACATACTCGAGTATGTGATCCTGGTCTG
ACGTGTTCT 3' (Reverse) with target sequence being 5'

GAACACGTCAGACCAGGATCACATA 3'. 4T1 clones with *Slc16a1* (encoding MCT1) suppression were generated using purchased oligos from Origene (TR309405, target sequence: CTCAATGACATGTATGGAG ACTACAAATA) and following the manufacturer's recommendation. shMct1 #1 and shMct1 #2 denote two distinct clones, selected with 4 µg/ml puromycin and knockdown confirmed by qRT-PCR. Scrambled shRNA (Origene) was used as control.

4T1 orthotopic mammary cancer models—Adult virgin female mice (~8 weeks of age, BALB/c, RRID:IMSR_CRL:028) were used for orthotopic implantation of 1×10^6 4T1 mammary epithelial cancer cells (single or bilateral tumors). For this, mice were anesthetized with ketamine/xylazine or isoflurane, the skin was incised, and cancer cells were implanted into the mammary fat pad (MFP). In the admix experiment, 5×10^5 4T1 cells were coinjected in a 1:1 ratio with 5×10^5 fibroblasts into the MFP of nu/nu mice. When the average combined tumor volume reached ~400-500 mm³ (~12-13 days post cancer cell implantation, see Figure S2B for individual experiments), α SMA-vTK and WT control mice received daily intraperitoneal (i.p.) injections with 50 mg/kg of ganciclovir (GCV, Thermo Fisher, 82410-32-0). Tumors were measured every 2 to 3 days using Vernier callipers. Mice were euthanized when the average tumor volume reached 1500 to 2000 mm³ in the control groups (~21-26 days post cancer cell implantation). For measurement of 4T1 tumor metabolites in α SMA-vTK and WT control, mice were sacrificed at day 18 post cancer cell implantation. When probing for glycolytic fibroblasts in different tumor stages, mice were sacrificed when tumors reached ~50-80 mm³, ~150-250 mm³, ~400-500 mm³, ~700-900 mm³, and ~1200-1500 mm³, respectively. For each stage, tumors from 4-6 mice were obtained. At time of sacrifice, mice were injected with hypoxyprom to probe for pimonidazole adduct formation in tumor tissues. To ascertain metastatic burden in lungs of mice with a tumor volume of ~400 mm³, 1×10^6 4T1 cells were injected in the right mammary fat pad and volume was monitored until sacrifice when tumor volume reached ~400 mm³. To measure α SMA and FSP1 expression in animal tissues, *α SMA-RFP* mice

(LeBleu et al., 2013a) were crossed to *S100A4-GFP* mice (Iwano et al., 2002) and subsequently implanted with 4T1 carcinoma cells as described above. 5 μm sections from formalin fixed paraffin-embedded lung tissues were stained with hematoxylin and eosin. Slides were scanned using Aperio Digital Scanner (Department of Veterinary Medicine and Surgery at MDACC). Alternatively, pictures were taken from the entire left lobe of the lung at original magnification $\times 2.5$ and reconstructed using Photoshop CS4 Photomerge application for quantification. Metastases were identified by histopathological analysis and metastatic area was quantified with Aperio eSlide Manager and Aperio Image Scope v12.3.2.8013 or NIH ImageJ software as a percentage of total (reconstructed) lung area. In some experiments, number of lung surface nodules were counted after sacrifice. Metastatic burden of 4T1 cancer cells was also assessed by quantitative PCR analysis for the 4T1 cancer cell-associated *GFP* gene using genomic DNA in one experiment (Trial 3, see Figure S2B).

While performing tumor measurements and lung metastasis analysis, the operator was blinded to the experimental groups the mice were stratified into or to their genotypes.

4T1 intravenous injections in $\alpha\text{SMA-vTK}$ mice— 0.5×10^6 4T1 mammary carcinoma cells were injected intravenously (retroorbital route) in $\alpha\text{SMA-vTK}$ and WT control mice. GCV treatment was started 2 days prior cancer cell injection and continued until the endpoint of the experiment (10 days after cancer cell injection). Quantification of lung metastatic burden was performed as described above.

MMTV-PyMT mammary cancer mouse models—MMTV-PyMT (Pymt) transgenic mice spontaneously develop tumors at 8-12 weeks of age in their mammary fat pads (Lin et al., 2003). For studies on tumor progression, mice were sacrificed when tumors reached a combined volume of approximately 800 mm^3 . The single tumors were measured, harvested and paraffin embedded. In total, 24 tumors from 11 distinct mice were used for analyses. For depletion studies, Pymt mice were crossed to $\alpha\text{SMA-vTK}$ mice to obtain Pymt; $\alpha\text{SMA-vTK}$ transgenic mice. In these animals, GCV treatment was started when the combined tumor volume reached $\sim 500 \text{ mm}^3$ and continued until endpoint of the experiment (20 days post GCV treatment start). For the transplantation experiments, Pymt mice were sacrificed when combined tumor volume reached $\sim 1000 \text{ mm}^3$. Individual tumors were collected and tumors of $\sim 0.6 \text{ g}$ were chosen for transplantation. These were cut into small pieces of $\sim 1 \text{ mm}^3$ and implanted into the right mammary fat pads of recipient $\alpha\text{SMA-vTK}$ and WT mice (one piece/fat pad). Each donor tumor was distributed to five recipient mice. GCV treatment was started once the tumor volumes exceeded 300 mm^3 in recipient mice and continued until the endpoint of the experiment (20 days post GCV treatment start). Quantification of lung metastatic burden in both models was performed as described above.

Immunofluorescence and immunohistochemistry—For human tissues, 5 μm cryosections were fixed in acetone at 4°C for 5 minutes (min). After incubating with blocking solution (1% BSA in PBS) for 20 min at room temperature (RT), primary antibodies against extracellular matrix proteins or other stromal markers were applied followed by FITC-conjugated secondary antibodies. Subsequently, sections were incubated with a CK8 antibody, which was visualized by Cy3-anti-rat IgG secondary antibody.

Sections were incubated with individual antibodies for 1 hour (h) at RT. For staining with α SMA and CAIX, primary α SMA antibody was followed by Cy3-conjugated secondary antibody incubation. For the subsequent incubation with CAIX antibody, a FITC-conjugated secondary antibody was used. The following primary antibodies were used: CK8 (Throma-1; the University of Iowa, 1:50), Collagen I (SouthernBiotech 1310-01; 1:200), Collagen III (SouthernBiotech 1330-01; 1:200), Laminin 1 (Sigma L9393; 1:200), Tenascin C (Abcam ab108930; 1:200), α SMA (Sigma F3777; 1:200), FSP1 (a gift from Dr. Eric Neilson, Vanderbilt Univ.; 1:500), CD31 (DAKO, JC70A; 1:50), CAIX (Novus Biologicals NB100-417; 1:100) and NG2 (Millipore AB5320; 1:200). FITC anti-goat IgG (Jackson ImmunoResearch 705-095-147; 1:200), FITC anti-rabbit IgG (Jackson ImmunoResearch 711-095-152; 1:200), Rhodamine anti-rabbit IgG (Jackson ImmunoResearch 711-295-152; 1:200), FITC anti-rat IgG (Jackson ImmunoResearch 712-095-153; 1:200), and Rhodamine anti-rat IgG (Jackson ImmunoResearch 712-295-153; 1:200) secondary antibodies were utilized. The slides were washed with PBS three times for 10 min and mounted with Vectashield plus DAPI (Vector Laboratories, H-1200). Staining was visualized on a Zeiss AxioSkop 2 fluorescent microscope and the images were taken with Axiovision Rel 4.8 software.

OCT-embedded tissues from *α SMA-RFP;S100A4-GFP* mice were fixed with acetone at 4°C for 5 min, before slides were mounted with Vectashield + DAPI. RFP and GFP expression was visualized using Zeiss AxioSkop 2 fluorescent microscope. Immunohistochemistry on paraffin-embedded mouse tissues for α SMA and Hypoxyprobe was performed using the Vector M.O.M. kit (Vector Laboratories, BMK-2202). Slides were deparaffinized, rehydrated and microwaved for 15 min at 98°C in citrate buffer (pH 6), before incubated with Hydrogen-peroxide (Fisher H325-100; 15 min at RT). Tissues were blocked with M.O.M. blocking reagent (prepared according to manufacturer's recommendations) for 30 min at RT, before incubated with primary antibody (α SMA DAKO M0851; 1:100, or Hypoxyprobe HPI Inc., 1:50) over night at 4°C. After washing 3x3 min with tris-buffered saline (TBS), secondary antibody (part of M.O.M. kit) incubation followed for 30 min at RT. Subsequently, slides were washed (TBS, 3x 3 min) and incubated with ABC reagent (Vector Laboratories, VECTASTAIN® Elite® ABC HRP Kit, PK-6100; prepared as recommended by manufacturer) for 30 min at RT. After another wash, incubation with DAB (Life Technologies, 750118) for 4 min at RT followed, before tissues were counter stained with Hematoxylin (30 s incubation, Sigma-Aldrich GHS316-500ML). Slides were dehydrated before coverslipping. Immunolabeling of α SMA and Hypoxyprobe has also previously been described (Keskin et al., 2015; Özdemir et al., 2014).

Immunofluorescence stainings on paraffin-embedded mouse tissues were performed using Tyramide Signal Amplification (TSA) technology (Perkin Elmer) as previously described (Carstens et al., 2017). In short, tissues were deparaffinized, rehydrated and microwaved for 15 min at 98°C in citrate buffer (pH 6) for antigen retrieval (AR; number of 15 min-long ARs varied by antibody; described below). After blocking with 1% BSA in TBST (Tris-buffered saline with Tween 20) for 10 min at RT, sections were incubated with primary antibody for 1 h at RT. A secondary antibody incubation followed using a horseradish peroxidase (HRP)-conjugated polymer (Biocare) for 10 min, before incubation with TSA reagent (Opal reagent, 1:50, Perkin Elmer; 10 min at RT). In between steps, slides were

washed with TBST 3x3 min. An additional antigen retrieval followed the immunolabeling to wash off antibodies. In case of co-immunolabeling with additional antibodies, the same procedure was repeated for each antibody. The following antibodies were used: CK8 (Throma-1; the University of Iowa, 1:50, 3 ARs), α SMA (DAKO M0851; 1:2000; 4 ARs), FBP1 (Abcam ab109020; 1:50; 2 ARs), PKM2 (Cell Signaling, CS #4053; 1:800, 2 ARs), HK2 (CS #2867; 1:200; 2 ARs), Lyve1 (Angio Bio Co 11-034; 1:100, 1 AR), GLUT1 (Abcam ab115730, 1:200, 4 ARs), CAIX (Novus Biologicals NB100-417; 1:1000; 2 ARs with Tris-EDTA buffer, pH 9.0, 0.05% Tween (TE buffer)).

Co-immunolabeling of tissues for CD31, PDGRFb and α SMA was performed in a similar procedure, without usage of TSA technology. Tissue sections were subjected to a 30 min AR using TE buffer before blocking with 4% Aurion Cold Water Fish Skin Gelatine (Electron Microscopy Sciences, 25560) for 1 h at RT. Incubation with primary antibodies: CD31 (Dianova, DIA 310; 1:400), α SMA (DAKO M0851; 1:400), PDGFR β (Thermo Fisher, MA5-15143; 1:100) (1 h at RT) was followed by 30 min incubation with secondary antibodies: goat anti-rabbit Alexa Fluor (Thermo Fisher, A11034, 1:250), donkey anti-mouse Alexa Fluor (Thermo Fisher, A31571, 1:250), goat anti-rat Alexa Fluor (Thermo Fisher, A11007, 1:250). All immunofluorescence labeling experiments were followed by a 5-minute incubation with DAPI (Life Technologies, D1306) before mounted using Fluoroshield mounting media (Sigma Aldrich, F618). Immunofluorescence images were acquired either with Vectra Multispectral Imaging System version 2 (Perkin Elmer), or Zeiss AxioSkop 2. Stainings on human and mouse tissues were quantified as described in Quantification and Statistical Analysis section.

Quantitative real time PCR—Primers were used with Power SYBR Green PCR Master Mix (Thermo Fisher, 4367659), in a 7300 Sequence Detector System (Applied Biosystems) and measurements were standardized to expression of the housekeeping genes, either acidic ribosomal phosphoprotein PO (ARP/36B4), β -actin or 18S. Fold-change in gene expression was determined using the ddCt method. Technical triplicates were used, and statistical analyses computed on the dCt that compared biological replicates (cell lines from distinct mice or biopsies). Primer sequences are listed in Table S3.

Primer set for measurement of GFP DNA—F 5'-TTTTTGTGATGCTCGTCAGG-3'; R 5'-AGGGGATAACGCAGGAAAGA-3'

Metabolomics—Metabolomics were performed with targeted mass spectrometry. For cultured cells, 4 mL of 80% LC-MS grade methanol were added to each 10 cm dish and incubated at -80°C for 15 min. Cells were scraped and collected from the tissue culture dish to be centrifuged at full speed for 5 min at 4°C to pellet cell debris and proteins. Supernatants were saved. Pellets were resuspended in 500 μL 80% methanol by vortexing and subsequently centrifuged as before. The supernatant was collected and pellet resuspension was repeated. The three extracted supernatants were pooled for a drying step. For tissues, 400 mL of 80% LC-MS grade methanol was added per 1-2 mg weight and homogenized for 30 s at -80°C then centrifuged at 14,000 rpm for 10 min at 4°C . Supernatants were collected and the steps from the beginning were repeated twice. Supernatants from all three extractions were pooled and centrifuged a final time at 14,000

rpm for 10 min at 4°C. Metabolite supernatants were dried by SpeedVac. Samples were re-suspended using 20 µL HPLC grade water for mass spectrometry. Between 120 and 285 endogenous water-soluble metabolites including some in both positive and negative ion mode were analyzed by a 5500 QTRAP triple quadrupole mass spectrometer (AB/Sciex) coupled to a Prominence UFLC HPLC system (Shimadzu) via selected reaction monitoring (SRM). The tissues were either weighted to ensure equal mass of starting material for metabolite extraction, or the protein concentration was measured on lysed tissues and the values were normalized accordingly. Peak intensity values were log-transformed and heatmaps were created from all predicted metabolites involved in human and mouse metabolic pathways, as determined by KEGG pathway analysis and/or human metabolome data base (HMDB). Note that color of the heatmap indicates the relative abundance of a given metabolite across samples. The source data (Mendeley dataset: <https://doi.org/10.17632/9dgjv8bt8c.1>) contains the full lists in the order the metabolites are listed in heatmaps. Metabolites were included in Figures 1L and 4F when up- or downregulation was consistent across samples within each experimental group (log₂ ratio or % metabolite change in experimental group was consistently up- or consistently downregulated compared to the average of the control samples).

Quantification of lactate—L-Lactate Assay Kit was purchased from Eton Bioscience Inc. and used per manufacturer's instructions. Cells were plated at the same number and volume. Culture media were collected 72 h later and were diluted 1:10 with ddH₂O prior to adding assay solution. Concentrations of lactate in samples were determined with the standard curve as a reference. Cell numbers counted at the time of medium harvest were used for normalization. For this assay, culture conditions of cells were not changed; the cells were cultured in RPMI-1640 media containing 20% fetal bovine serum (FBS) with 100 U/ml penicillin/streptomycin and 250 ng/ml amphotericin (PSA) (complete media).

Immunoblotting—Cells were lysed with RIPA buffer using standard protocol. Protein concentrations were determined by BCA Protein Assay (Thermo Fisher, 23225; or Micro BCA, Thermo Fisher, 23235) with a microplate reader at 562 nm. Lysates were run on 10% polyacrylamide gels and proteins transferred onto PVDF membranes overnight. Membranes were blocked with 5% milk in TBST. Antibodies detecting β-Actin (Sigma Aldrich, A3854), HIF1-α (Novus Biologicals, AF1935) and β-Tubulin (Abcam) were used at recommended dilutions for either 4 h at RT or overnight at 4°C on shaker. Appropriate HRP-conjugated secondary antibodies (Sigma) were used at 1:10,000 dilution for 1 h at RT on shaker. Membranes were exposed to GenDEPOT PICO ECL solution (Thermo Fisher, 50-101-5479) prior to film exposure. The intensity of the bands from uncropped blots was quantified using ImageJ software. The areas underneath peak for the proteins of interest were normalized to those of actin/tubulin in each blot.

For HIF-1α western blot shown in Figure 7A, Wes system (Protein Simple) was utilized and assay was performed according to manufacturer's recommendations with the following antibodies: HIF-1α antibody (Novus Biologicals, AF1935, 1:10), β-Actin (Sigma Aldrich, A3854, 1:100). Band intensities were quantified using the Compass Software (Protein

Simple). For HIF1- α , arrows in Data S2 point to the bands quantified. Uncropped blots are shown in Data S2.

MeDIP and bisulfite conversion analyses—Methylated DNA was isolated from 1.0 μ g of sonicated DNA using Methylamp Methylated DNA Capture (MeDIP) Kit. DNA was added to each antibody-coated well and incubated for 120 min at RT on an orbital shaker. After releasing with proteinase K for 1 h at 65°C, DNA was eluted from the column and adjusted to a final volume of 100 μ l with nuclease-free water. For each sample, an input vial was performed using total sonicated DNA for further normalization. For DNA amplification, 5 μ L of eluted DNA was added to the reaction mixture containing the primer pair (300 nmol/l each), a ROX passive reference dye (Bio-Rad, 1725858) and diluted 2x SYBR green Supermix (Bio-Rad, 170880) in a final volume of 25 μ l for each PCR reaction. The real-time PCR reactions were performed in a 96-well reaction plate using the Mx3000P QPCR System (Stratagene, Santa Clara, USA). The PCR reaction was stopped when the fluorescent signal increased over the threshold and electrophoresis of PCR products were done on a Bioanalyzer 2100 (Agilent Technologies, Santa Clara, USA).

Primer sequences:

FBP1 F 5' CGAGCGCTGCGGACACTCGGG 3'

R 5' CGCACCGCCGAAGAGATGGC 3'

PKM1/2 F 5' CTACTCTGAGGCATTGCTCTGC 3'

R 5' CCGGGTGTCTGCTCTGGCGCAC 3'

HIF1A F 5' GGAGAAAGAGAGCAGGAGCATTAC 3'

R 5' GCTCGTCTGTGTTTAGCGGCGGAGG 3'

LDHA F 5' CGGTAGGGCCCTGCGCGCACGGCG 3'

R 5' CACGGAGCCCACCTCTCGAGCGTC 3'

Primer sequences for additional *HIF1A* promoter regions in Figure S6:

HIF1A non CPG F 5' GGGCCAGAGCGAGACTCCGCC 3'

R 5' GTGTCTATAACCACAGTATTATGG 3'

HIF1A CPG1 F 5' CAAGGTGAGTCCCCTGTGCTCC 3'

R 5' CTCTGCTGGGCTCTCTGTTC 3'

HIF1A CPG2 F 5' GGAGAAAGAGAGCAGGAGCATTAC 3'

R 5' GCTCGTCTGTGTTTAGCGGCGGAGG 3'

Clones following bisulfite conversion from each sample were aligned and displayed as box graphs.

5-Azacytidine treatments of hBFs—hBFs were seeded in 10 cm plates (100,000 cells/plate). 3 days after seeding media was replaced with media containing 3 μM 5-Azacytidine (Sigma Aldrich, A2385-250MG). Media was replaced with fresh 5-Azacytidine containing media after 24 h. After 48 h, cells were harvested. hBF # 33 and # 38 were used in 3 independent experiments (biological replicates) and hBF #120 was used in 2 independent experiments (biological replicates).

^{13}C glucose labeling experiments—hCAFs were incubated in media (10% FBS (dialyzed, Thermo Scientific), 2 mM L-glutamine (GIBCO), 2.5 mM $^{13}\text{C}_6$ glucose in glucose-free DMEM) containing uniformly ^{13}C labeled glucose ([U- ^{13}C] glucose, Cambridge Isotope Laboratories, CLM1396) for 48 h to allow labeling of all glucose-derived metabolites in the cells. The cells were washed four times with PBS and processed for mass spectrometry as described above, or, after incubation in media containing [U- ^{13}C] glucose, washed three times with PBS to remove any residual [U- ^{13}C] glucose before incubation with media containing unlabeled glucose (10% FBS, 2 mM L-glutamine, 2.5 mM glucose in DMEM) to collect conditioned media (CM), which contained labeled secreted metabolites. The CM metabolites were extracted and measured (as described above) or the CM was fed to MDA-MB-231 cells for 24 h. MDA-MB-231 cells were then washed four times with PBS and processed for mass spectrometry as described above. Schematic representations of the experimental design ($n = 1$ dish of cells in each condition) are shown in Figures 5A and 5B. Unlabeled MDA-MB-231 cells, as well as unlabeled hCAFs served as controls. If false positive rate in controls exceeded 5% (for metabolites secreted by hCAFs, Figure 5C) or 10% (for metabolites in hCAFs and MDA-MB-231 cells, Figures 5A and 5D), metabolites were excluded.

Seahorse Glycolysis Stress Test—Glycolysis stress tests were performed using a Seahorse XF96 analyzer (Agilent). The assays were performed according to manufacturer's instructions. Specifically, microplates (part of Seahorse XFe96 FluxPak, Agilent, 102416-100) were coated with 10 $\mu\text{g}/\text{ml}$ rat tail Collagen I (Corning 354249) before mouse fibroblasts (10,000 cells/well) and human fibroblasts (8000 cells/well) were seeded. Assays were performed 2 days after seeding to allow cells to attach to the plate. 24 h before the assay, cartridge (part of Seahorse XFe96 FluxPak, Agilent, 102416-100) was filled with H_2O and placed in a non- CO_2 incubator. After overnight incubation, H_2O was replaced with Calibrant (part of Seahorse XFe96 FluxPak, Agilent, 102416-100), and placed back in a non- CO_2 incubator for at least one hour prior to the assay. Seahorse XF prep station was used to replace cell culture media with Base Media (Agilent, 102353-100) supplemented with 2mM Glutamine (GIBCO; pH of media adjusted to 7) 45 min prior to the assay. After media change, cells were placed in non- CO_2 incubator. 10 min before start of the assay, medium was replaced once again (with Base Media containing Glutamine) using Seahorse XF prep station, to ensure correct baseline readings. Assay was performed with a standard protocol: for each stage, 3 measurements were taken; for each measurement, media was mixed for 3 min and the measurement lasted 4 min. After baseline measurements, glucose (10 mM final

concentration, Seahorse XF Glycolysis Stress Test Kit, Agilent 103020-100) was injected from port A. After 3 measurements, Oligomycin (3 μ M final concentration, Seahorse XF Glycolysis Stress Test Kit, Agilent 103020-100) was injected from port B and measurements were repeated. Lastly, 2 deoxy-glucose (100 mM final concentration, Seahorse XF Glycolysis Stress Test Kit, Agilent 103020-100) was injected from port C and 3 measurements followed before assay ended. Data was analyzed with Seahorse Wave software. After the assay, cells were fixed to the plates with 4% paraformaldehyde (Electron Microscopy Sciences 15710-S) and stained with DAPI (Life Tech). Subsequently, pictures were taken of each well (5 pictures in 20x magnification) and % DAPI positive area was quantified with ImageJ software to determine cell density, which was used to normalize ECAR values. Glycolysis, glycolytic capacity and glycolytic reserve were determined as recommended in the Seahorse XF User Manual: *Glycolysis*: last rate measurement before glucose injection is subtracted from the max rate measurement before oligomycin injection. *Glycolytic capacity*: last rate measurement before glucose injection is subtracted from the max rate after oligomycin injection. *Glycolytic reserve*: glycolysis is subtracted from glycolytic capacity.

QUANTIFICATION AND STATISTICAL ANALYSIS

The sample sizes for each experiment are indicated in the figures (different dots in graphs) as well as in figure legends.

For comparison between two groups, a one-tailed or two-tailed unpaired t test or Mann-Whitney test was performed, as listed in the figure legend. When appropriate, a paired t test was used (indicated in figure legend). For comparison between three groups, an ordinary one-way ANOVA test was used. A *P value* < 0.05 was used to define statistical significance. *P values* are indicated in all graphs. For details also see source data (Mendeley dataset: <https://doi.org/10.17632/9dgjv8bt8c.1>).

Immunohistochemistry and immunofluorescence—Immunofluorescence stainings of human tissue was quantified as follows: FITC staining and stromal area were quantified in 3 to 5 visual fields per sample using the NIH ImageJ Analysis Software, where the same threshold was used for all compared conditions. Collagen I, III and tenascin C staining was determined as a ratio of FITC staining signal/ stromal area for each visual field. Laminin1 staining was assessed as a ratio of FITC signal/perimeter length around tumor or epithelial structures. CD31, NG2, α SMA and FSP1 positive cells only within the stroma were quantified as a ratio of individual marker positive cell number/ stromal area per visual field. In case of NG2-covered microvessels (CD31⁺), the numbers were calculated as a percentage out of all microvessels per visual field. CAIX/ α SMA double positive cells were quantified as percentage of total number of α SMA⁺ cells.

Quantification of immunohistochemistry and immunofluorescence on mouse tissues was based on established methods in the laboratory either as percent (of area or positive cells) or as immunoreactive scores (IRS) depending on the specific immunolabeling (method indicated in figures). IRS were obtained from the sum of distribution and intensity scores for each section, established on a scale of 1 to 4 (or adapted to 1-5 or 1-3, depending on the

respective experiment). Scores were based on expression of a single marker, or co-labeling (as stated in respective figure legends) (Meyerholz and Beck, 2018). Tumor histology, rather than size was taken into consideration in all quantification methods. 4T1 tumors are highly necrotic in their center, and this is further exacerbated with tumor size. Pymt tumors are less necrotic, although necrosis also increases with increasing tumor volume. When comparing any two experimental groups, only non-necrotic areas with live tissue were taken into consideration and quantified. In the case of 4T1 tumors, most of the tissue areas used for quantification were in the tumor periphery, and areas in tumor center were only quantified if no necrosis was identified (live tissue). When quantifying immunolabeling in different tumor volumes (Figures S7D and S7E), the same parameters were applied, excluding necrotic areas in the quantifications shown. Immunofluorescence labeling for α SMA and Ki67 in Figure S4D included other markers, such as epithelial, endothelial and mesenchymal markers. For quantification, only α SMA single positive cells as well as α SMA/Ki67 double positive cells were quantified as percentage out of all fibroblasts (CK8-CD31-). Quantification of immunolabeling in Figure 7F was done in non-necrotic areas that were specifically hypoxic (CAIX-positive) or normoxic (CAIX-negative), respectively. Here, CAFs positive for α SMA and HK2/PKM2/FBP1 (respectively) were quantified in hypoxic (CAIX high) versus normoxic (CAIX low) areas. In case of α SMA/FBP1, only small tumors (n = 5) were taken into consideration, as very low FBP1 expression was detected in large tumors. VSL and LMB quantified IRS scores and were blinded to genotype or experimental groups. All quantifications were performed with the same microscope settings, or using pictures taken with identical exposure settings. Quantifications were carried out on images that were equally adjusted for brightness and contrast, and the entire image was adjusted. In some cases, brightness and contrast were further adjusted to generate the representative images in the figures, and such adjustments were done equally on the entire image.

Supplementary Material

Refer to Web version on PubMed Central for supplementary material.

ACKNOWLEDGMENTS

The Kalluri laboratory was/is supported by the National Cancer Institute (NCI) (CA125550, CA155370, and CA15192) and the Cancer Prevention and Research Institute of Texas (CPRIT). Additional support includes 5P01CA120964-05 and 5P30CA006516-46 from the NCI to J.M.A.; the Harvard Clinical and Translational Science Center training grant to A.P.V.; the Department of Defense Breast Cancer Research Predoctoral Traineeship Award (W81XWH-09-1-0008) to J.T.O.; the NIH Research Training Grant in Gastroenterology (2T32DK007760-11) to V.S.L.; and the Rosalie Hite Fellowship at the University of Texas MD Anderson Cancer Center (MDACC) to L.M.B. The Metabolomics Core Facility at MDACC is supported by CPRIT grant RP130397 and NIH grants S10OD012304-01, U01CA235510, and P30CA016672. We thank M. Esteller and J.F. Carmona Sanz for help with bisulfite sequencing, P. Phillips for help with immunohistochemistry, Y. Chen for advice on lymphatic immunolabeling, and F.L. Muller for helpful discussions regarding metabolic labeling studies.

REFERENCES

- Albregues J, Bertero T, Grasset E, Bonan S, Maiel M, Bourget I, Philippe C, Herraiz Serrano C, Benamar S, Croce O, et al. (2015). Epigenetic switch drives the conversion of fibroblasts into proinvasive cancer-associated fibroblasts. *Nat. Commun* 6, 10204. [PubMed: 26667266]
- Alkaskas T, Moyano-Galceran L, Arsenian-Henriksson M, and Lehti K (2018). Fibroblasts in the Tumor Microenvironment: Shield or Spear? *Int. J. Mol. Sci* 19, E1532. [PubMed: 29883428]

- Ammirante M, Shalpour S, Kang Y, Jamieson CA, and Karin M (2014). Tissue injury and hypoxia promote malignant progression of prostate cancer by inducing CXCL13 expression in tumor myofibroblasts. *Proc. Natl. Acad. Sci. USA* 111, 14776–14781. [PubMed: 25267627]
- Borriello L, Nakata R, Sheard MA, Fernandez GE, Sposto R, Malvar J, Blavier L, Shimada H, Asgharzadeh S, Seeger RC, and DeClerck YA (2017). Cancer-Associated Fibroblasts Share Characteristics and Protumorigenic Activity with Mesenchymal Stromal Cells. *Cancer Res.* 77, 5142–5157. [PubMed: 28687621]
- Branco MR, Ficiz G, and Reik W (2011). Uncovering the role of 5-hydroxymethylcytosine in the epigenome. *Nat. Rev. Genet* 13, 7–13. [PubMed: 22083101]
- Carstens JL, Correa de Sampaio P, Yang D, Barua S, Wang H, Rao A, Allison JP, LeBleu VS, and Kalluri R (2017). Spatial computation of intratumoral T cells correlates with survival of patients with pancreatic cancer. *Nat. Commun* 8, 15095. [PubMed: 28447602]
- Chaudhri VK, Salzler GG, Dick SA, Buckman MS, Sordella R, Karoly ED, Mohny R, Stiles BM, Elemento O, Altorki NK, and McGraw TE (2013). Metabolic alterations in lung cancer-associated fibroblasts correlated with increased glycolytic metabolism of the tumor. *Mol. Cancer Res* 11, 579–592. [PubMed: 23475953]
- Cooke VG, LeBleu VS, Keskin D, Khan Z, O’Connell JT, Teng Y, Duncan MB, Xie L, Maeda G, Vong S, et al. (2012). Pericyte depletion results in hypoxia-associated epithelial-to-mesenchymal transition and metastasis mediated by met signaling pathway. *Cancer Cell* 21, 66–81. [PubMed: 22264789]
- Costa A, Kieffer Y, Scholer-Dahirel A, Pelon F, Bourachot B, Cardon M, Sirven P, Magagna I, Fuhrmann L, Bernard C, et al. (2018). Fibroblast Heterogeneity and Immunosuppressive Environment in Human Breast Cancer. *Cancer Cell* 33, 463–479.e10. [PubMed: 29455927]
- de Kruijf EM, van Nes JG, van de Velde CJ, Putter H, Smit VT, Liefers GJ, Kuppen PJ, Tollenaar RA, and Mesker WE (2011). Tumor-stroma ratio in the primary tumor is a prognostic factor in early breast cancer patients, especially in triple-negative carcinoma patients. *Breast Cancer Res. Treat* 125, 687–696. [PubMed: 20361254]
- Dennison JB, Shahmoradgoli M, Liu W, Ju Z, Meric-Bernstam F, Perou CM, Sahin AA, Welm A, Oesterreich S, Sikora MJ, et al. (2016). High Intratumoral Stromal Content Defines Reactive Breast Cancer as a Low-risk Breast Cancer Subtype. *Clin. Cancer Res* 22, 5068–5078. [PubMed: 27172895]
- Diers AR, Broniowska KA, Chang CF, and Hogg N (2012). Pyruvate fuels mitochondrial respiration and proliferation of breast cancer cells: effect of monocarboxylate transporter inhibition. *Biochem. J* 444, 561–571. [PubMed: 22458763]
- Doherty JR, and Cleveland JL (2013). Targeting lactate metabolism for cancer therapeutics. *J. Clin. Invest* 123, 3685–3692. [PubMed: 23999443]
- Du H, and Che G (2017). Genetic alterations and epigenetic alterations of cancer-associated fibroblasts. *Oncol. Lett* 13, 3–12. [PubMed: 28123515]
- Fantozzi A, and Christofori G (2006). Mouse models of breast cancer metastasis. *Breast Cancer Res.* 8, 212. [PubMed: 16887003]
- Fiaschi T, Marini A, Giannoni E, Taddei ML, Gandellini P, De Donatis A, Lanciotti M, Serni S, Cirri P, and Chiarugi P (2012). Reciprocal metabolic reprogramming through lactate shuttle coordinately influences tumor-stroma interplay. *Cancer Res.* 72, 5130–5140. [PubMed: 22850421]
- Gui DY, Sullivan LB, Luengo A, Hosios AM, Bush LN, Gitego N, Davidson SM, Freinkman E, Thomas CJ, and Vander Heiden MG (2016). Environment Dictates Dependence on Mitochondrial Complex I for NAD⁺ and Aspartate Production and Determines Cancer Cell Sensitivity to Metformin. *Cell Metab.* 24, 716–727. [PubMed: 27746050]
- Guido C, Whitaker-Menezes D, Capparelli C, Balliet R, Lin Z, Pestell RG, Howell A, Aquila S, Andò S, Martinez-Outschoorn U, et al. (2012). Metabolic reprogramming of cancer-associated fibroblasts by TGF- β drives tumor growth: connecting TGF- β signaling with “Warburg-like” cancer metabolism and L-lactate production. *Cell Cycle* 11, 3019–3035. [PubMed: 22874531]
- Hu M, and Polyak K (2008). Microenvironmental regulation of cancer development. *Curr. Opin. Genet. Dev* 18, 27–34. [PubMed: 18282701]

- Huangyang P, and Simon MC (2018). Hidden features: exploring the non-canonical functions of metabolic enzymes. *Dis. Model. Mech* 11, dmm033365. [PubMed: 29991493]
- Iwano M, Plieth D, Danoff TM, Xue C, Okada H, and Neilson EG (2002). Evidence that fibroblasts derive from epithelium during tissue fibrosis. *J. Clin. Invest* 110, 341–350. [PubMed: 12163453]
- Kalluri R (2016a). The biology and function of exosomes in cancer. *J. Clin. Invest* 126, 1208–1215. [PubMed: 27035812]
- Kalluri R (2016b). The biology and function of fibroblasts in cancer. *Nat. Rev. Cancer* 16, 582–598. [PubMed: 27550820]
- Keskin D, Kim J, Cooke VG, Wu CC, Sugimoto H, Gu C, De Palma M, Kalluri R, and LeBleu VS (2015). Targeting vascular pericytes in hypoxic tumors increases lung metastasis via angiopoietin-2. *Cell Rep.* 10, 1066–1081. [PubMed: 25704811]
- Kim J, de Sampaio PC, Lundy DM, Peng Q, Evans KW, Sugimoto H, Gagea M, Kienast Y, Amaral NSD, Rocha RM, et al. (2016). Heterogeneous perivascular cell coverage affects breast cancer metastasis and response to chemotherapy. *JCI Insight* 1, e90733. [PubMed: 28018977]
- Koslowski M, Luxemburger U, Türeci O, and Sahin U (2011). Tumor-associated CpG demethylation augments hypoxia-induced effects by positive autoregulation of HIF-1 α . *Oncogene* 30, 876–882. [PubMed: 21042279]
- Koukourakis MI, Giatromanolaki A, Harris AL, and Sivridis E (2006). Comparison of metabolic pathways between cancer cells and stromal cells in colorectal carcinomas: a metabolic survival role for tumor-associated stroma. *Cancer Res.* 66, 632–637. [PubMed: 16423989]
- LeBleu VS, and Kalluri R (2018). A peek into cancer-associated fibroblasts: origins, functions and translational impact. *Dis. Model. Mech* 11, dmm029447. [PubMed: 29686035]
- LeBleu VS, and Neilson EG (2020). Origin and functional heterogeneity of fibroblasts. *FASEB J.* 34, 3519–3536. [PubMed: 32037627]
- LeBleu VS, Taduri G, O’Connell J, Teng Y, Cooke VG, Woda C, Sugimoto H, and Kalluri R (2013a). Origin and function of myofibroblasts in kidney fibrosis. *Nat. Med* 19, 1047–1053. [PubMed: 23817022]
- LeBleu VS, Teng Y, O’Connell JT, Charytan D, Müller GA, Müller CA, Sugimoto H, and Kalluri R (2013b). Identification of human epididymis protein-4 as a fibroblast-derived mediator of fibrosis. *Nat. Med* 19, 227–231. [PubMed: 23353556]
- Li B, Qiu B, Lee DS, Walton ZE, Ochocki JD, Mathew LK, Mancuso A, Gade TP, Keith B, Nissim I, and Simon MC (2014). Fructose-1,6-bi-sphosphatase opposes renal carcinoma progression. *Nature* 513, 251–255. [PubMed: 25043030]
- Liu EY, Jones JG, Li P, Zhu L, Whitney KD, Muller WJ, and Pollard JW (2003). Progression to malignancy in the polyoma middle T oncoprotein mouse breast cancer model provides a reliable model for human diseases. *Am. J. Pathol* 163, 2113–2126. [PubMed: 14578209]
- Lisanti MP, Martinez-Outschoorn UE, and Sotgia F (2013). Oncogenes induce the cancer-associated fibroblast phenotype: metabolic symbiosis and “fibroblast addiction” are new therapeutic targets for drug discovery. *Cell Cycle* 12, 2723–2732. [PubMed: 23860382]
- Liu VM, and Vander Heiden MG (2015). The Role of Pyruvate Kinase M2 in Cancer Metabolism. *Brain Pathol.* 25, 781–783. [PubMed: 26526946]
- Liu Q, Liu L, Zhao Y, Zhang J, Wang D, Chen J, He Y, Wu J, Zhang Z, and Liu Z (2011). Hypoxia induces genomic DNA demethylation through the activation of HIF-1 α and transcriptional upregulation of MAT2A in hepatoma cells. *Mol. Cancer Ther* 10, 1113–1123. [PubMed: 21460102]
- Liu Z, Chen X, Wang Y, Peng H, Wang Y, Jing Y, and Zhang H (2014). PDK4 protein promotes tumorigenesis through activation of cAMP-response element-binding protein (CREB)-Ras homolog enriched in brain (RHEB)-mTORC1 signaling cascade. *J. Biol. Chem* 289, 29739–29749. [PubMed: 25164809]
- Liu J, Mi J, and Zhou BP (2015). Metabolic rewiring in cancer-associated fibroblasts provides a niche for oncogenesis and metastatic dissemination. *Mol. Cell. Oncol* 3, e1056331. [PubMed: 27308568]
- Luo W, Hu H, Chang R, Zhong J, Knabel M, O’Meally R, Cole RN, Pandey A, and Semenza GL (2011). Pyruvate kinase M2 is a PHD3-stimulated coactivator for hypoxia-inducible factor 1. *Cell* 145, 732–744. [PubMed: 21620138]

- Madsen CD, Pedersen JT, Venning FA, Singh LB, Moeendarbary E, Charras G, Cox TR, Sahai E, and Erler JT (2015). Hypoxia and loss of PHD2 inactivate stromal fibroblasts to decrease tumour stiffness and metastasis. *EMBO Rep.* 16, 1394–1408. [PubMed: 26323721]
- Martinez-Outschoorn UE, Lisanti MP, and Sotgia F (2014). Catabolic cancer-associated fibroblasts transfer energy and biomass to anabolic cancer cells, fueling tumor growth. *Semin. Cancer Biol* 25, 47–60. [PubMed: 24486645]
- McFate T, Mohyeldin A, Lu H, Thakar J, Henriques J, Halim ND, Wu H, Schell MJ, Tsang TM, Teahan O, et al. (2008). Pyruvate dehydrogenase complex activity controls metabolic and malignant phenotype in cancer cells. *J. Biol. Chem* 283, 22700–22708. [PubMed: 18541534]
- Meyerholz DK, and Beck AP (2018). Principles and approaches for reproducible scoring of tissue stains in research. *Lab. Invest* 98, 844–855. [PubMed: 29849125]
- Micallef L, Vedrenne N, Billet F, Coulomb B, Darby IA, and Desmoulière A (2012). The myofibroblast, multiple origins for major roles in normal and pathological tissue repair. *Fibrogenesis Tissue Repair* 5 (Suppl 1), S5. [PubMed: 23259712]
- Migneco G, Whitaker-Menezes D, Chiavarina B, Castello-Cros R, Pavlides S, Pestell RG, Fatatis A, Flomenberg N, Tsigos A, Howell A, et al. (2010). Glycolytic cancer associated fibroblasts promote breast cancer tumor growth, without a measurable increase in angiogenesis: evidence for stromal-epithelial metabolic coupling. *Cell Cycle* 9, 2412–2422. [PubMed: 20562527]
- Mitchell MI, and Engelbrecht AM (2017). Metabolic hijacking: a survival strategy cancer cells exploit? *Crit. Rev. Oncol. Hematol* 109, 1–8. [PubMed: 28010894]
- Monteran L, and Erez N (2019). The Dark Side of Fibroblasts: Cancer-Associated Fibroblasts as Mediators of Immunosuppression in the Tumor Microenvironment. *Front. Immunol* 10, 1835. [PubMed: 31428105]
- Moorman AM, Vink R, Heijmans HJ, van der Palen J, and Kouwenhoven EA (2012). The prognostic value of tumour-stroma ratio in triple-negative breast cancer. *Eur. J. Surg. Oncol* 38, 307–313. [PubMed: 22264965]
- O’Connell JT, Sugimoto H, Cooke VG, MacDonald BA, Mehta AI, LeBleu VS, Dewar R, Rocha RM, Brentani RR, Resnick MB, et al. (2011). VEGF-A and Tenascin-C produced by S100A4+ stromal cells are important for metastatic colonization. *Proc. Natl. Acad. Sci. USA* 108, 16002–16007. [PubMed: 21911392]
- Orimo A, Gupta PB, Sgroi DC, Arenzana-Seisdedos F, Delaunay T, Naeem R, Carey VJ, Richardson AL, and Weinberg RA (2005). Stromal fibroblasts present in invasive human breast carcinomas promote tumor growth and angiogenesis through elevated SDF-1/CXCL12 secretion. *Cell* 121, 335–348. [PubMed: 15882617]
- Özdemir BC, Pentcheva-Hoang T, Carstens JL, Zheng X, Wu CC, Simpson TR, Laklai H, Sugimoto H, Kahlert C, Novitskiy SV, et al. (2014). Depletion of carcinoma-associated fibroblasts and fibrosis induces immunosuppression and accelerates pancreas cancer with reduced survival. *Cancer Cell* 25, 719–734. [PubMed: 24856586]
- Pavlides S, Whitaker-Menezes D, Castello-Cros R, Flomenberg N, Witkiewicz AK, Frank PG, Casimiro MC, Wang C, Fortina P, Addya S, et al. (2009). The reverse Warburg effect: aerobic glycolysis in cancer associated fibroblasts and the tumor stroma. *Cell Cycle* 8, 3984–4001. [PubMed: 19923890]
- Pavlova NN, and Thompson CB (2016). The Emerging Hallmarks of Cancer Metabolism. *Cell Metab.* 23, 21–41.
- Rankin EB, and Giaccia AJ (2016). Hypoxic control of metastasis. *Science* 352, 175–180. [PubMed: 27124451]
- Rattigan YI, Patel BB, Ackerstaff E, Sukenick G, Koutcher JA, Glod JW, and Banerjee D (2012). Lactate is a mediator of metabolic cooperation between stromal carcinoma associated fibroblasts and glycolytic tumor cells in the tumor microenvironment. *Exp. Cell Res* 318, 326–335. [PubMed: 22178238]
- Romero IL, Mukherjee A, Kenny HA, Litchfield LM, and Lengyel E (2015). Molecular pathways: trafficking of metabolic resources in the tumor microenvironment. *Clin. Cancer Res* 21, 680–686. [PubMed: 25691772]

- Roy A, and Bera S (2016). CAF cellular glycolysis: linking cancer cells with the microenvironment. *Tumour Biol.* 37, 8503–8514. [PubMed: 27075473]
- Sanford-Crane H, Abrego J, and Sherman MH (2019). Fibroblasts as Modulators of Local and Systemic Cancer Metabolism. *Cancers (Basel)* 11, E619. [PubMed: 31058816]
- Semenza GL (2010). HIF-1: upstream and downstream of cancer metabolism. *Curr. Opin. Genet. Dev* 20, 51–56. [PubMed: 19942427]
- Stincone A, Prigione A, Cramer T, Wamelink MM, Campbell K, Cheung E, Olin-Sandoval V, Grüning NM, Krüger A, Tauqeer Alam M, et al. (2015). The return of metabolism: biochemistry and physiology of the pentose phosphate pathway. *Biol. Rev. Camb. Philos. Soc* 90, 927–963. [PubMed: 25243985]
- Sugimoto H, Mundel TM, Kieran MW, and Kalluri R (2006). Identification of fibroblast heterogeneity in the tumor microenvironment. *Cancer Biol. Ther* 5, 1640–1646. [PubMed: 17106243]
- Tchou J, Kossenkov AV, Chang L, Satija C, Herlyn M, Showe LC, and Purè E (2012). Human breast cancer associated fibroblasts exhibit subtype specific gene expression profiles. *BMC Med. Genomics* 5, 39. [PubMed: 22954256]
- Tchou J, Zhang PJ, Bi Y, Satija C, Marjundar R, Stephen TL, Lo A, Chen H, Mies C, June CH, et al. (2013). Fibroblast activation protein expression by stromal cells and tumor-associated macrophages in human breast cancer. *Hum. Pathol* 44, 2549–2557. [PubMed: 24074532]
- Trimboli AJ, Cantemir-Stone CZ, Li F, Wallace JA, Merchant A, Creasap N, Thompson JC, Caserta E, Wang H, Chong JL, et al. (2009). Pten in stromal fibroblasts suppresses mammary epithelial tumours. *Nature* 461, 1084–1091. [PubMed: 19847259]
- Tyan SW, Kuo WH, Huang CK, Pan CC, Shew JY, Chang KJ, Lee EY, and Lee WH (2011). Breast cancer cells induce cancer-associated fibroblasts to secrete hepatocyte growth factor to enhance breast tumorigenesis. *PLoS One* 6, e15313. [PubMed: 21249190]
- Vander Heiden MG, and DeBerardinis RJ (2017). Understanding the Intersections between Metabolism and Cancer Biology. *Cell* 168, 657–669. [PubMed: 28187287]
- Wang HJ, Hsieh YJ, Cheng WC, Lin CP, Lin YS, Yang SF, Chen CC, Izumiya Y, Yu JS, Kung HJ, and Wang WC (2014). JMJD5 regulates PKM2 nuclear translocation and reprograms HIF-1 α -mediated glucose metabolism. *Proc. Natl. Acad. Sci. USA* 111, 279–284. [PubMed: 24344305]
- Whitaker-Menezes D, Martinez-Outschoorn UE, Lin Z, Ertel A, Flomenberg N, Witkiewicz AK, Birbe RC, Howell A, Pavlides S, Gandara R, et al. (2011). Evidence for a stromal-epithelial “lactate shuttle” in human tumors: MCT4 is a marker of oxidative stress in cancer-associated fibroblasts. *Cell Cycle* 10, 1772–1783. [PubMed: 21558814]
- Zhang D, Wang Y, Shi Z, Liu J, Sun P, Hou X, Zhang J, Zhao S, Zhou BP, and Mi J (2015). Metabolic reprogramming of cancer-associated fibroblasts by IDH3 α downregulation. *Cell Rep.* 10, 1335–1348. [PubMed: 25732824]

Highlights

- Pro-glycolytic CAFs fuel cancer cell metabolism to support breast tumor growth
- CAFs attain a pro-glycolytic phenotype by epigenetic control of glycolysis
- Chronic hypoxia enables epigenetic reprogramming of glycolysis in fibroblasts

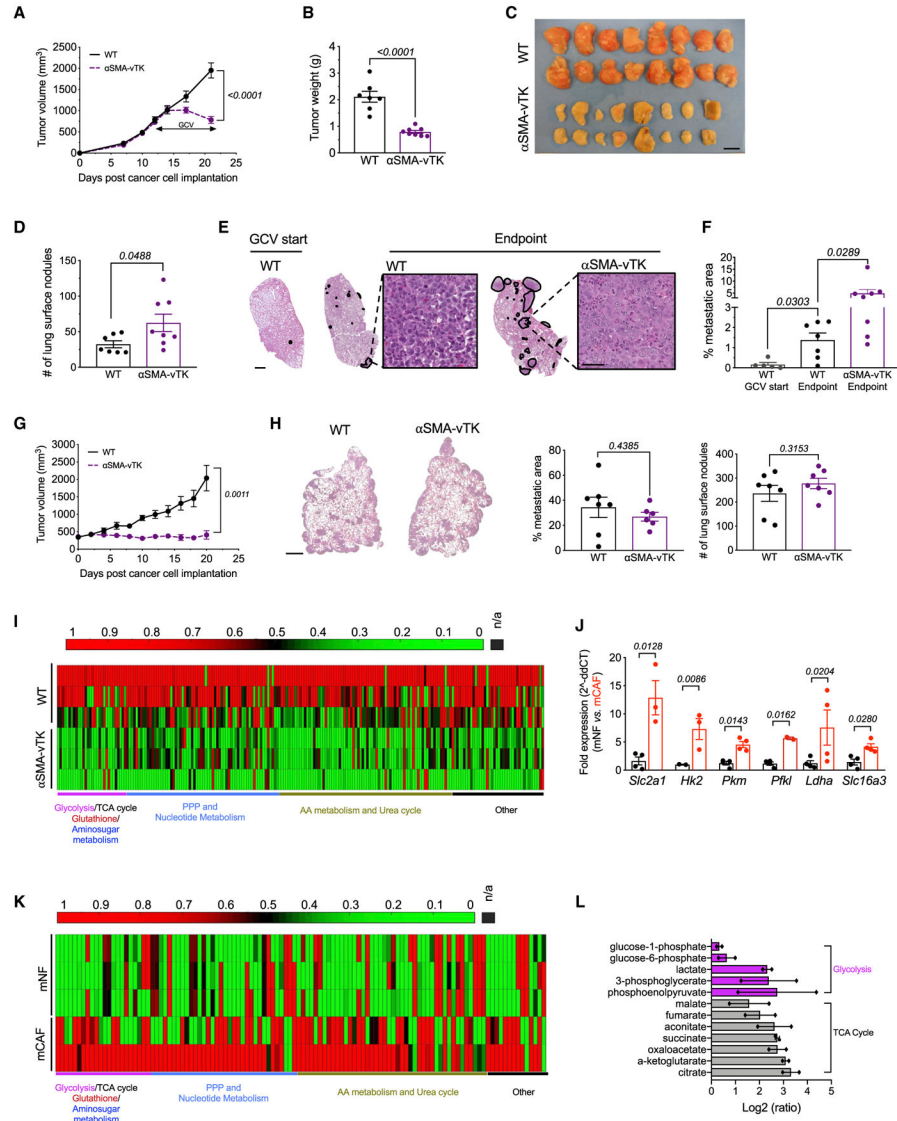


Figure 1. α SMA⁺ CAFs Display Enhanced Glycolytic Activity and Promote Primary Tumor Growth

(A) 4T1 orthotopic tumor growth in WT and α SMA-vTK mice. GCV start: day 12 post-4T1 implantation. WT, n = 7; α SMA-vTK, n = 8 mice.

(B) Tumor weight at endpoint.

(C) 4T1 tumors from WT (top) and α SMA-vTK (bottom) mice (tumors from trial 1, see Figure S2B). Scale bar: 10 mm.

(D) Number of lung surface nodules at endpoint.

(E) Representative H&E-stained lung sections with metastases outlined in black. Lungs from endpoint in (A) and from mice with 4T1 tumor burden of \sim 400 mm³ (GCV start). Scale bar, whole lung: 1 mm; scale bar, magnified image: 50 μ m.

(F) Percentage of metastatic burden computed from H&E-stained lung sections, Mann-Whitney test. Lungs at GCV start, n = 5.

(G) Tumor growth in WT and α SMA-vTK mice implanted with Pymt tumors from GCV start (tumor volume $>300 \text{ mm}^3$). WT, n = 7, α SMA-vTK, n = 10 mice.

(H) Quantification of lung metastatic burden and count of lung surface nodules in WT and α SMA-vTK mice injected intravenously with 4T1 cells. Scale bar: 2 mm.

(I) Metabolite accumulation in α SMA-vTK tumors and WT tumors from n = 3 mice per group (tumors from trial 6; Figure S2B).

(J) Transcript levels of key metabolic enzymes in mNFs and mCAFs; n = 2–4 distinct mice, 1-tailed unpaired t test, or Mann-Whitney test.

(K and L) All metabolites (K) and selected metabolites (L) in mCAFs compared to mNFs. mNFs, n = 3 distinct mice; mCAFs, n = 2 distinct mice.

Statistics in (A) and (G) performed on tumor volumes at endpoint. Data in (A), (B), and (F) also shown in trial 4 (Figure S2B). The data are presented as means or means \pm SEMs.

Individual dots in graphs depict distinct mice. Unless otherwise indicated, 2-tailed unpaired t test was used. p values are indicated in all of the graphs. GCV, ganciclovir; mCAFs: murine cancer-associated fibroblasts; mNFs, murine normal fibroblasts; n/a, not available (no metabolite captured); PPP, pentose phosphate pathway; TCA, tricarboxylic acid cycle; WT, wild-type.

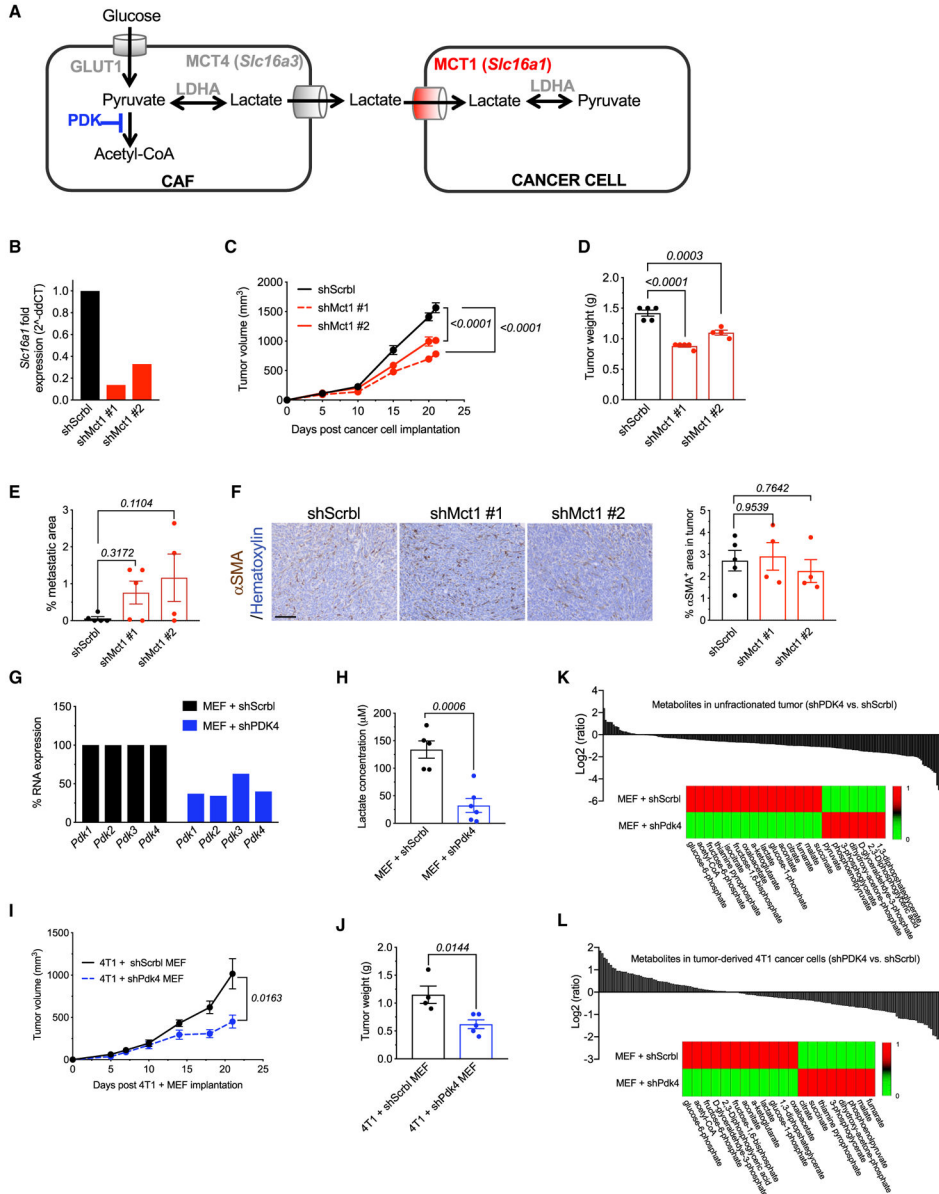


Figure 2. CAFs and Cancer Cells Demonstrate Metabolic Cooperation to Promote Tumor Growth

(A) Schematic of CAFs-cancer cells lactate shuttle.

(B) *Slc16a1* (MCT1) expression in 4T1 cells with control (shScrbl) and *Slc16a1* shRNA knockdowns (shMct1 #1 and shMct1 #2). n = 1 per cell line (average of 3 technical replicates).

(C) Orthotopic tumor growth of 4T1 shScrbl (n = 5 mice), 4T1 shMct1 #1 (n = 5 mice) and 4T1 shMct1 #2 (n = 4 mice) cells.

(D) Tumor weights of indicated experimental groups (endpoint).

(E) Percentage of metastatic burden computed from H&E stained lung sections.

(F) Representative α SMA immunolabeling in tumors in the indicated groups with quantification. Scale bar: 100 μ m.

(G) Gene expression for the indicated genes in shScrbl MEF and shPdk4 MEF. n = 1 per cell line (average of 3 technical replicates).

(H) Lactate secretion of the indicated cells. n = 5–6 distinct wells of cells.

(I) Tumor volume measurements. 4T1 + shScrbl MEF, n = 4; 4T1 + shPdk4 MEF, n = 5 mice.

(J) Tumor weight from endpoint in (I).

(K and L) Relative metabolite accumulation in 4T1 + shPdk4 MEF tumors (K) and FACS-purified cancer cells (L) compared to control 4T1+ shScrbl MEF tumors and FACS-purified cancer cells. n = 1 tumor per group (K), and n = 1 pool of 4T1 cells from n = 4 4T1 + shScrbl MEF and n = 5 4T1 + shPdk4 MEF tumors (L).

Heatmap shows the metabolites involved in glycolysis and the TCA cycle.

Statistics in (C) and (I) performed on tumor volumes at endpoint. The data are presented as means or means \pm SEMs. Individual dots in graphs depict distinct mice. 2-tailed unpaired t test (H–J) or 1-way ANOVA (C–F), p values are indicated in all of the graphs. MEF, murine embryonic fibroblasts.

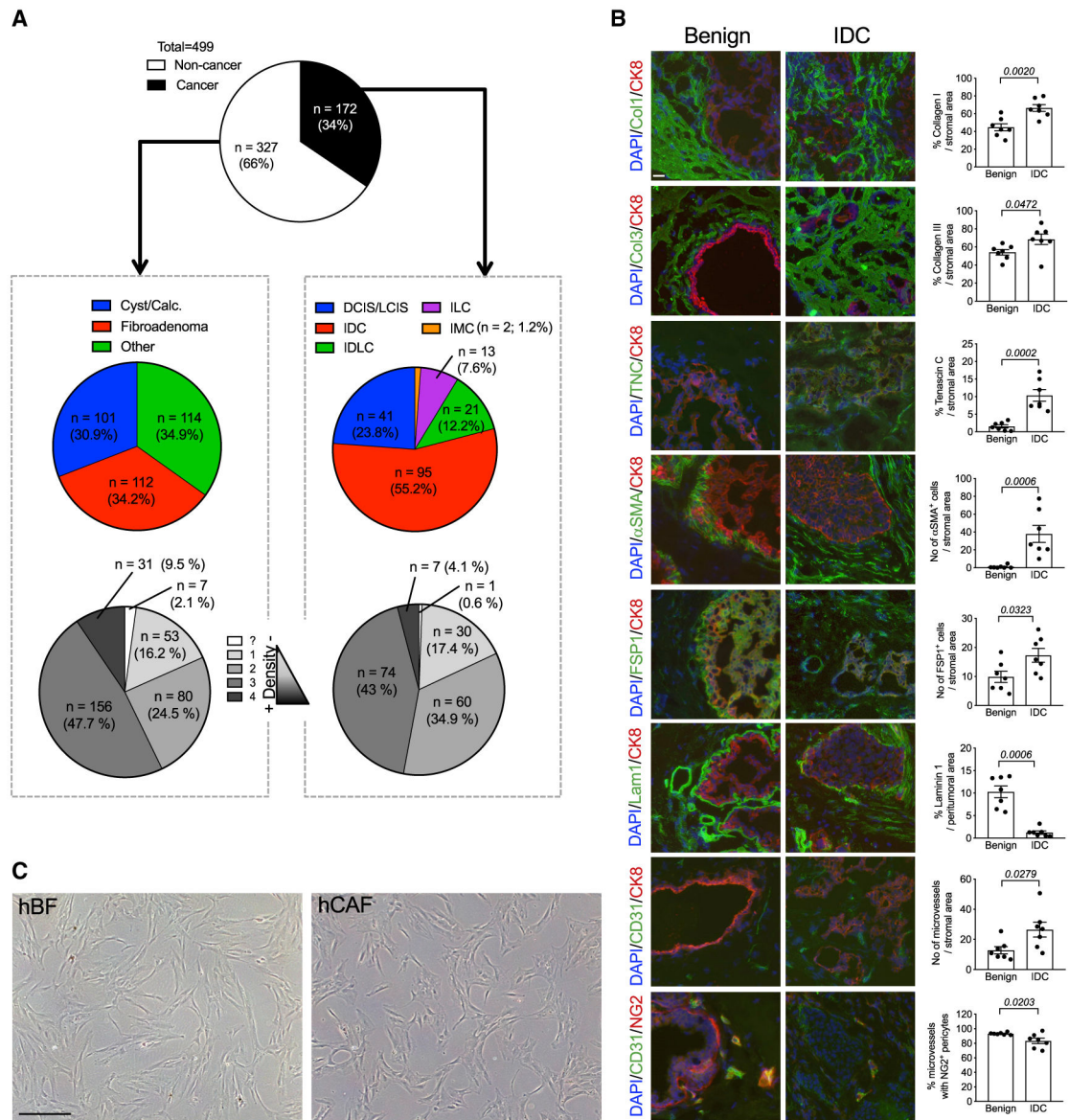


Figure 3. Heterogeneity in Breast Cancer Biopsies Used to Generate hBFs and hCAFs
 (A) Distribution of pathological findings and mammographic densities of breast tissue biopsies (n = 499). See also Table S1.

(B) Representative immunostaining of benign and IDC tissue sections for the listed antigens with quantitation. Single-color channels were altered individually based on background signal to enhance images. Scale bar: 20 μm. n = 7 cases per group.

(C) Representative pictures of fibroblasts isolated from benign and cancer tissues. Scale bar: 200 μm.

The data are presented as means or means ± SEMs. Individual dots in graphs depict distinct patient tissues. 2-tailed unpaired t test or Mann-Whitney test; p values are indicated in all of the graphs. Calc, calcification; DCIS/LCIS, ductal/lobular cancer *in situ*; hBFs, human benign (breast) fibroblasts; hCAFs: human breast cancer-associated fibroblasts; IDC,

invasive ductal carcinoma; IDLC, invasive ductal-lobular carcinoma; IMC, invasive mammary carcinoma.

Author Manuscript

Author Manuscript

Author Manuscript

Author Manuscript

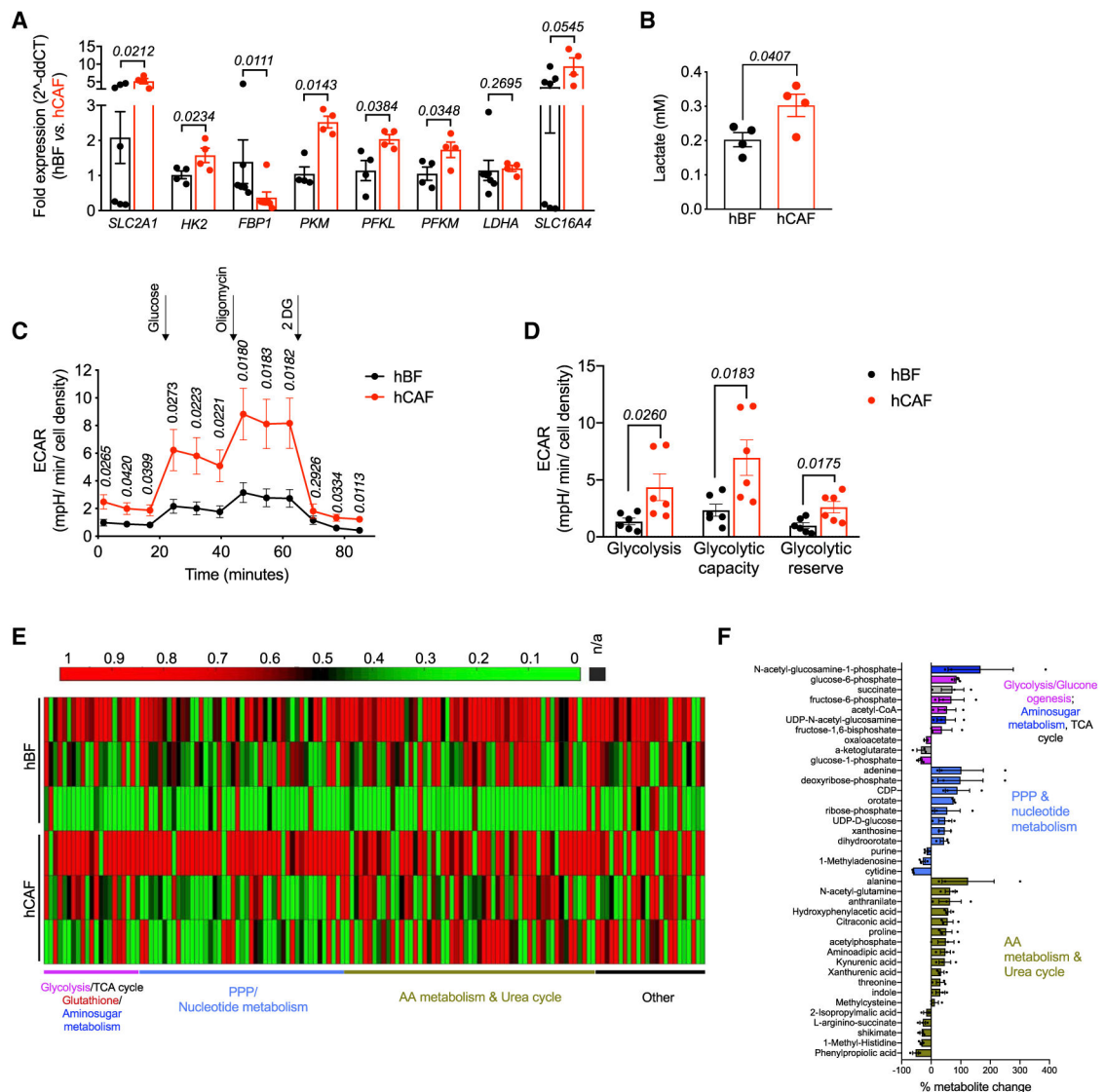


Figure 4. hCAFs Are Pro-glycolytic Compared to Fibroblasts from Benign Lesions

(A) Gene expression for the indicated genes in hBFs and hCAFs. hBFs, $n = 4-6$ distinct cases; hCAFs, $n = 4$ distinct cases, 1-tailed unpaired t test, or Mann-Whitney test.

(B) Lactate secretion in hBFs and hCAFs. $n = 4$ distinct cases per group.

(C) Glycolysis stress test. Arrows indicate the addition of glucose (20 min), oligomycin (42 min), and 2DG (65 min). $n = 6$ distinct cases of hCAFs and hBFs.

(D) Measurements of glycolysis, glycolytic capacity, and reserve for the cell lines in (C). Calculations are described in STAR Methods.

(E and F) Heatmap of all detected metabolites (E) and changes in metabolite accumulation (F) in hCAFs compared to hBFs. hBFs, $n = 3$ distinct cases; hCAFs, $n = 3$ distinct cases.

The data are presented as means or means \pm SEMs. Individual dots depict fibroblasts from distinct patients. p values are indicated in all of the graphs. 2-tailed unpaired t test or Mann-Whitney test, unless otherwise indicated. aa metabolism, amino acid metabolism; ECAR, extracellular acidification rate; hBFs, human benign (breast) fibroblasts; hCAFs, human

(breast) cancer-associated fibroblasts; n/a, not available (no metabolite captured); PPP, pentose phosphate pathway; 2DG, 2-deoxy-glucose; TCA, tricarboxylic acid cycle.

Author Manuscript

Author Manuscript

Author Manuscript

Author Manuscript

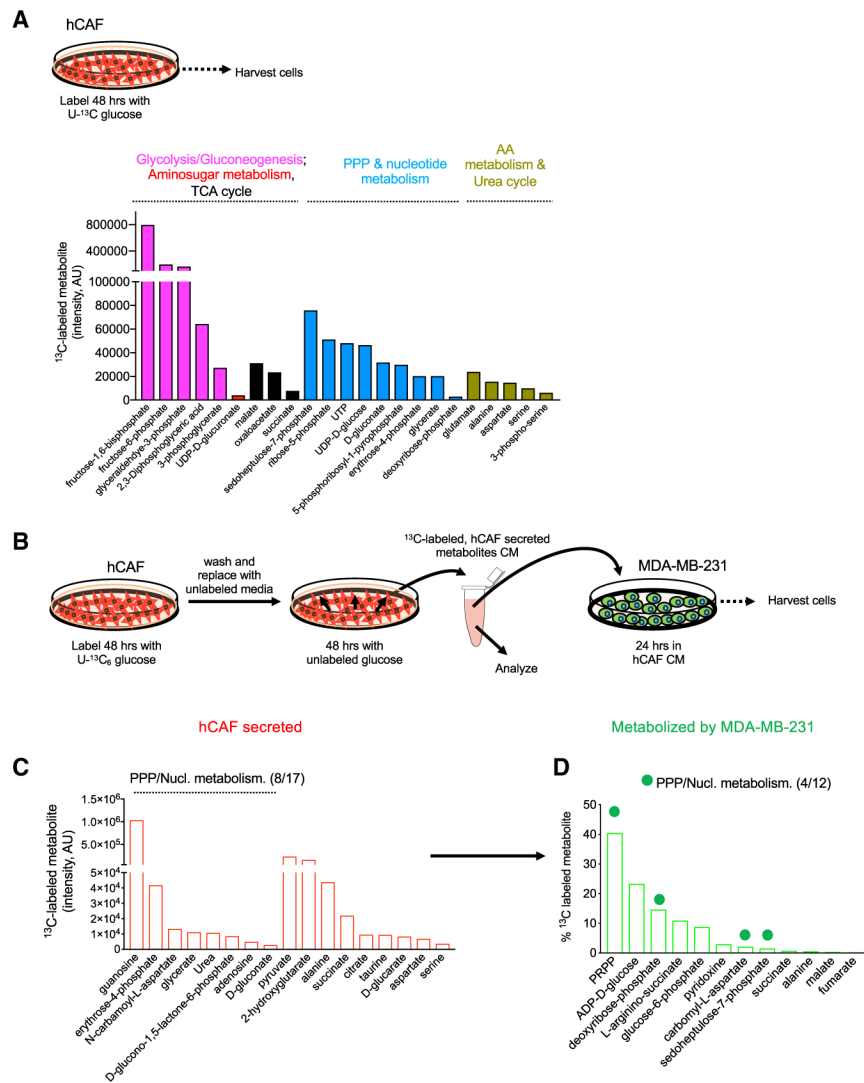


Figure 5. CAF-Secreted Metabolites Fuel the Biosynthetic Pathways of Cancer Cells

(A) [U-¹³C] glucose-derived metabolites in hCAFs (48 h incubation). n = 1 case.

(B) Experimental setup (see STAR Methods for details).

(C) Top 17 hCAF-secreted ¹³C labeled metabolites (n = 1 case; 8/17 indicates 8 out of the 17 secreted metabolites are part of PPP and nucleotide metabolism).

(D) Top 12 ¹³C-labeled metabolites in MDAMB231 cells after uptake (n = 1; 4/12 indicates 4 of the 12 secreted metabolites are part of PPP and nucleotide metabolism).

Green dots: metabolites associated with PPP and nucleotide metabolism. CM, conditioned media; hCAFs, human breast cancer-associated fibroblasts; Nucl. metabolism, nucleotide metabolism; PPP, pentose phosphate pathway.

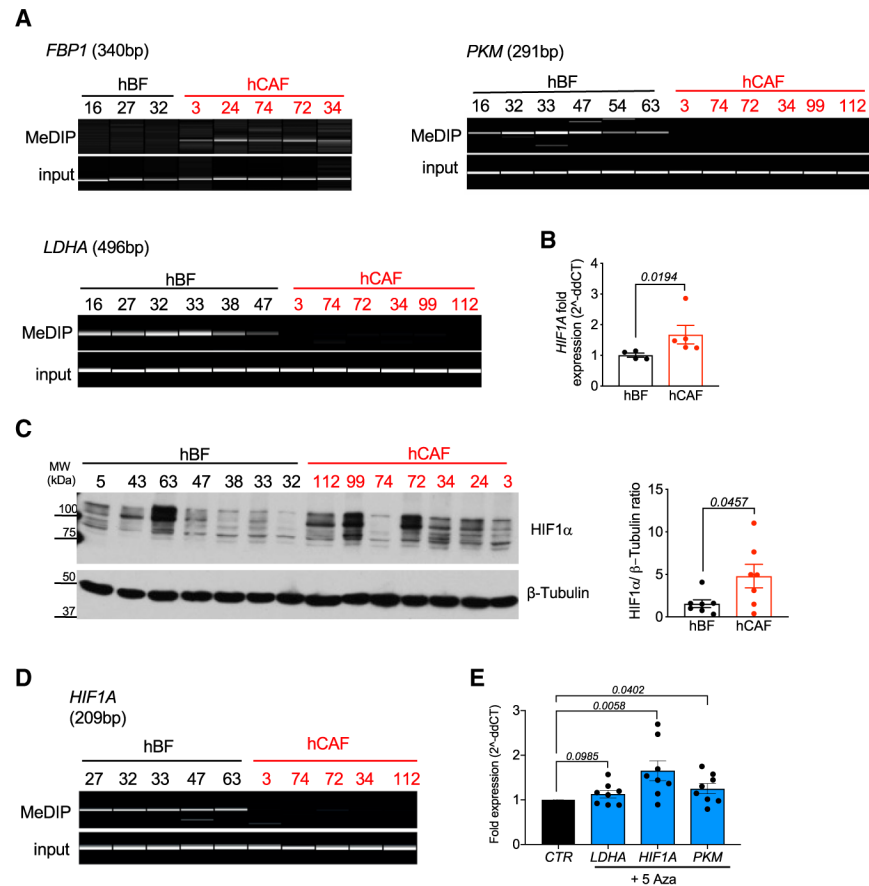


Figure 6. Differential DNA Methylation of Rate-Limiting Glycolytic Enzyme Genes in hCAFs

(A) Methylation status of *PKM*, *FBP1*, and *LDHA* in hBFs and hCAFs.

(B) *HIF1A* gene expression in hBFs (n = 4 distinct cases) and hCAFs (n = 5 distinct cases), 1-tailed unpaired t test.

(C) HIF-1 α and β -Tubulin protein levels, 2-tailed unpaired t test.

(D) Methylation status of *HIF1A* in hBFs and hCAFs.

(E) Expression of indicated genes in hBFs untreated (black bar) and treated with 5-Aza (blue bars). For each gene, data were normalized to baseline expression when untreated. hBFs from 3 distinct patients in 3 independent experiments were used (total of 8 biological replicates, as 1 line was only used for 2 distinct experiments). Paired 1-tailed t tests.

The numbers in the graphs denote the fibroblast line (case ID). Individual dots in graphs depict fibroblasts from distinct patients. The data are presented as means or means \pm SEMs. 5-Aza, 5-azacytidine; hBFs, human benign (breast) fibroblasts; hCAFs, human (breast) cancer-associated fibroblasts.

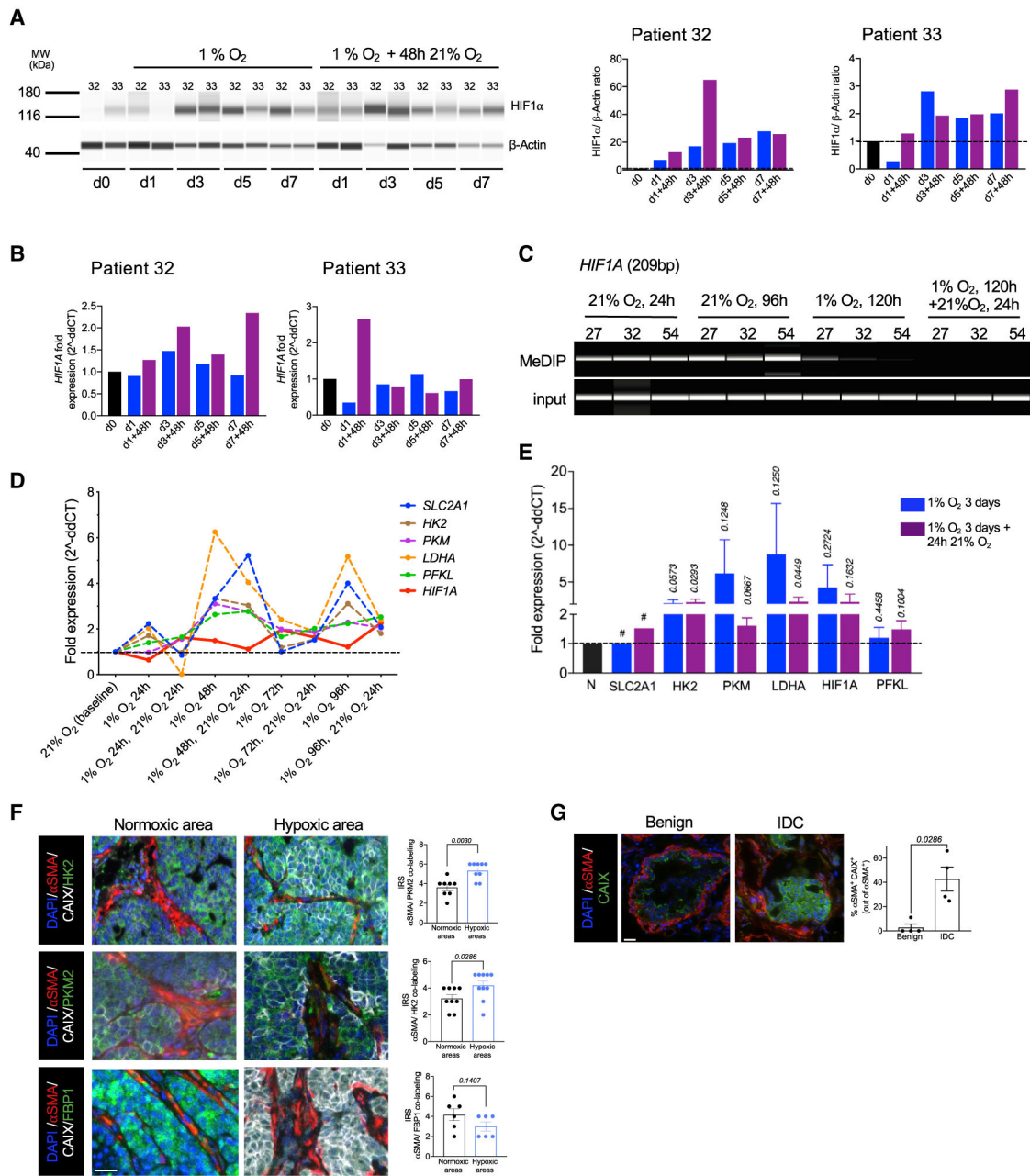


Figure 7. Chronic Hypoxia Is Sufficient to Promote Stable Upregulation of HIF-1α Stabilized by Epigenetic Rewiring

(A) hBFs from n = 2 cases (#32 and #33) were cultured in increasing durations of hypoxia with or without subsequent 48-h periods of re-oxygenation (21% O₂). HIF-1α and β-Actin protein levels in the described conditions characterized by western blot and associated quantification. The dotted line denotes baseline expression in 21% O₂ (day 0).

(B) *HIF1A* gene expression in the described conditions.

(C) Methylation status of *HIF1A* gene in hBFs subjected to the indicated conditions (27, 32, and 54 represent patient numbers; see Tables S1 and S2).

(D) Relative mRNA expression of glycolytic genes in hBFs subjected to increasing periods of hypoxia; each time point followed by re-oxygenation. $n = 1$ hBF (#21). The experiment was performed in 6-well plates with 3 wells per condition (technical replicates). For the qPCR, each replicate was plated in duplicates, which for analysis were averaged (see source data).

(E) Expression of indicated genes in hBFs cultured in hypoxia for 3 days, followed by 24 h of re-oxygenation. $n = 3$ distinct patients (#21, #43, #129; see Table S2); data for patient #21 also shown in (D). Dotted line indicates baseline expression in 21% O_2 . 1-tailed paired t tests or Wilcoxon matched-pairs signed-rank test.

(F) Immunolabeling of Pymt tumors for CAIX and α SMA together with HK2 (top panel), PKM2 (center panel), and FBP1 (bottom panel). Ten distinct tumors from the experiment in Figure S7D were used for quantification. Mann-Whitney test.

(G) Immunolabeling for CAIX and α SMA with quantification. $n = 4$ benign and 4 cancer tissues. Mann-Whitney test. Single-color channels were altered individually based on background signal to enhance images.

The data are presented as means or means \pm SEMs. Individual dots depict tissues from distinct mice or patients. d0, d1, (...), d7, day 0, day 1, (...), day 7; Hypoxia, 1% O_2 ; IRS, immunoreactive score; MW, molecular weight; N, normoxia (21% O_2); #, no statistical analysis, because *SLC2A1* expression was only measured in patient #21. p values are indicated in all of the graphs.

KEY RESOURCES TABLE

REAGENT or RESOURCE	SOURCE	IDENTIFIER
Antibodies		
α SMA	Sigma Aldrich	Cat# F3777; RRID:AB_476977
α SMA	DAKO	Cat# M0851; RRID:AB_2313736
β -Actin	Sigma Aldrich	Cat# A3854; RRID:AB_262011
CAIX	Novus Biologicals	Cat# NB100-417; RRID:AB_10003398
CD31	DAKO	Cat# JC70A; RRID:AB_2114471
CD31	Dianova	Cat # DIA 310; RRID:AB_2631039
CK8 (Throma-1)	the University of Iowa	n/a
Collagen I	SouthernBiotech	Cat# 1310-01; RRID:AB_2753206
Collagen III	SouthernBiotech	Cat# 1330-01; RRID:AB_2794734
FSP1	Dr. Eric Neilson, Vanderbilt Univ	n/a
FBP1	Abcam	Cat# ab109020; RRID:AB_10865049
GLUT1	Abcam	Cat# ab115730; RRID:AB_10903230
HIF1 α	Novus Biologicals	Cat# AF1935; RRID:AB_355064
HK2	Cell Signaling	Cat# CS #2867; RRID:AB_2232946
Hypoxyprobe	HPI Inc.	Cat# HP1-100; RRID:AB_2811309
Laminin 1	Sigma Aldrich	Cat# L9393; RRID:AB_477163
Lyve1	Angio Bio Co	Cat# 11-034; RID:AB_2813732
NG2	Millipore	Cat# AB5320; RRID:AB_91789
PDGFR β	Thermo Fisher	Cat# MA5-15143; RRID:AB_10985851
PKM2	Cell Signaling	Cat# 4053; RRID:AB_1904096
Tenascin C	Abcam	Cat# ab108930; RRID:AB_10865908
Donkey anti-mouse Alexa Fluor	Thermo Fisher	Cat# A31571; RRID:AB_162542
FITC anti-goat IgG	Jackson ImmunoResearch	Cat# 705-095-147; RRID:AB_2340401
FITC anti-rabbit IgG	Jackson ImmunoResearch	Cat# 711-095-152; RRID:AB_2315776
FITC anti-rat IgG	Jackson ImmunoResearch	Cat# 712-095-153; RRID:AB_2340652
Goat anti-rabbit Alexa Fluor	Thermo Fisher	Cat# A11034; RRID:AB_2576217
Goat anti-rat Alexa Fluor	Thermo Fisher	Cat# A11007; RRID:AB_10561522
Rhodamine anti-rabbit IgG	Jackson ImmunoResearch	Cat# 711-295-152; RRID:AB_2340613
Rhodamine anti-rat IgG	Jackson ImmunoResearch	Cat# 712-295-153; RRID:AB_2340676
Biological Samples		
Human breast biopsies	Brigham and Women's Hospital Boston	N/A
Chemicals, Peptides, and Recombinant Proteins		
Ganciclovir	Thermo Fisher	82410-32-0
5-Azacytidine	Sigma Aldrich	A2385-250MG

REAGENT or RESOURCE	SOURCE	IDENTIFIER
[U- ¹³ C] glucose	Cambridge Isotope Laboratories	CLM-1396-PK
Hydrogen Peroxide	Fisher Scientific	H325-100
DAB	Life Technologies	750118
DAPI	Life Technologies	D1306
Hematoxylin	Sigma-Aldrich	GHS316-500ML
Aurion Cold Water Fish Skin Gelatine	Electron Microscopy Sciences	25560
Fluoroshield mounting media	Sigma Aldrich	F618
Vectashield Mounting Media with DAPI	Vector Laboratories	H1200
GenDEPOT PICO ECL SOLUTION	Thermo Fisher	501015479
RoxPassiveReference dye	BioRad	1725858
SYBR Green Supermix	BioRad	170880
Power SYBR Green PCR Master Mix	Thermo Fisher	4367659
Paraformaldehyde	Electron Microscopy Sciences	15710-S
Critical Commercial Assays		
VECTASTAIN® Elite® ABC HRP Kit	Vector Laboratories	PK-6100
M.O.M. Immunodetection kit	Vector Laboratories	BMK-2202
L-Lactate Assay kit	Eton Bioscience Inc	1200011002
BCA Protein Assay kit	Thermo Fisher	23225
Micro BCA Protein Assay kit	Thermo Fisher	23235
Seahorse XFe96 FluxPak	Agilent	102416-100
Seahorse XF Glycolysis Stress Test Kit	Agilent	103020-100
Deposited Data		
Source Data	Mendeley dataset	https://doi.org/10.17632/9dgjv8bt8c.1
Experimental Models: Cell Lines		
4T1 (modified to express GFP and Luciferase)	ATCC	CRL-2539 RRID:CVCL_0125
MMTV-PyMT derived primary fibroblasts	Isolated in study	N/A
4T1 orthotopic tumor-derived primary fibroblasts	Isolated in study	N/A
Healthy mammary fat pads murine fibroblasts	Isolated in study	N/A
Human breast biopsy derived fibroblasts	Isolated in study	N/A
Mouse embryonic fibroblasts	Isolated in study (BALB/c)	N/A
Human: MDA-MB-231	ATCC	HTB-26; RRID:CVCL_0062
Experimental Models: Organisms/Strains		
Mouse: BALB/c	Charles River	RRID:IMSR_CRL:028
Mouse: αSMA-RFP (backcrossed to BALB/c background)	Kalluri laboratory (available at Jackson Laboratory)	RRID:IMSR_JAX:031160
Mouse: MMTV-PyMT (backcrossed to BALB/c in Kalluri lab)	Jackson Laboratory	RRID:IMSR_JAX:022974
Mouse: nu/nu	Charles River	RRID:IMSR_CRL:088
Mouse: αSMA-vTK (backcrossed to BALB/c background)	Kalluri laboratory (available at Jackson Laboratory)	RRID:IMSR_JAX:029921
Mouse: S100A4-GFP	Eric Neilson laboratory (available at Jackson Laboratory)	RRID:IMSR_JAX:012893
Oligonucleotides		

REAGENT or RESOURCE	SOURCE	IDENTIFIER
shRNA targeting Pdk4: 5' CCGGTCTACTCTATGTCAGG TTATGCTCGAGCATAACCTGAC ATAGAGTAGATTTTGG 3' Forward	This paper	N/A
shRNA targeting Pdk4: 5' AATTCAAAAATCTACTCTATG TCAGGTTATGCTCGAGCATAAC CTGACATAGAGTAGA 3' Reverse	This paper	N/A
shScrbl control for Pdk4: 5' CCGGGAACACGTCAGACCAG GATCACATACTCGAGTATGTGAT CCTGGTCTGACGTGTCTTTTGG 3' Forward	This paper	N/A
shScrbl control for Pdk4: 5' AATTCAAAAAGAACACGTCAG ACCAGGATCACATACTCGAGTA TGTGATCCTGGTCTGACGTGTTC 3' Reverse	This paper	N/A
Forward primer for measurement of GFP DNA: 5'- TTTTTGTGATGCTCGTCAGG-3'	This paper	N/A
Reverse primer for measurement of GFP DNA: 5'- AGGGGATAACGCAGGAAAGA-3'	This paper	N/A
Primers for qPCR analyses can be found in Table S3	This paper	N/A

Author Manuscript

Author Manuscript

Author Manuscript

Author Manuscript